Higher-Order System Identification and Control Design for a Coaxial Rotorcraft

Barzin Hosseini*

Georgia Institute of Technology, Atlanta, Georgia 30332 Jared A. Grauer[†]

NASA Langley Research Center, Hampton, Virginia 23681 Florian Holzapfel[‡] •

Technical University of Munich, 85748 Garching, Germany

Juergen Rauleder§

Georgia Institute of Technology, Atlanta, Georgia 30332

https://doi.org/10.2514/1.C038157

The edm aerotec CoAX 600 rotorcraft was converted to an uncrewed aerial vehicle at the Technical University of Munich. In this work, a higher-order physics-based model of the system was identified based on flight test data and blade element momentum theory (BEMT). The paper describes the higher-order model structure and the system identification techniques used in the process. The validated model was used for control design and pilot training purposes. The simulation model consists of a physics-based model structure developed by coupling a dynamic rotor model with a rigid-body fuselage. Aerodynamic models for both the fuselage and the coaxial rotors contain unknown parameters that were estimated based on flight test data using a Maximum-Likelihood parameter estimation method in the time domain. The nonlinear model was linearized in hover, and the linearized model was used for control design and stability analysis. The design and validation of the flight controller are also discussed in the paper. The physics-based model allows for the comprehensive interpretation of the estimated parameters and the involved aerodynamic phenomena. Furthermore, it reduces the number of parameters estimated from flight data.

Nomenclature						
C_L, C_D, C_Q	=	wind-axis nondimensional aerodynamic lift,				
		drag, and side force coefficients				
C_l, C_m, C_n	=	body-axis nondimensional aerodynamic roll-,				
		pitch-, and yaw-moment coefficients				
c_{β}	=	correction factor for rotor model cyclic inputs				
$\stackrel{c_{eta}}{C_{R_l}}$	=	rotor blade section (two-dimensional) lift coef-				
		ficient				
$egin{array}{c} C_{R_d} \ C_T \end{array}$	=	rotor blade section drag coefficient				
C_T	=	helicopter thrust coefficient				
D_R	=	rotor diameter, m				
\boldsymbol{F}	=	aerodynamic or rotor forces (depending on the				
		index), N				
$(I^G)_{BB}$	=	helicopter inertia matrix (excluding the blades)				
		in body-fixed frame, $kg - m^2$				
M	=	aerodynamic or rotor moments (depending on				
		the index), N-m				
M_{eta}	=	rotor hinge moment, N-m				
p, q, r	=	roll, pitch, and yaw rate of the helicopter, rad/s				
$ar{q}$	=	dynamic pressure, N/m ²				

A part of this work was Presented as Paper 2024-1717 at the AIAA			
SciTech 2024 Forum, Orlando, FL, January 8-12, 2024; received 28 July			
2024; accepted for publication 4 February 2025; published online 11 April			
2025. Copyright © 2025 by Barzin Hosseini, Jared Grauer, Florian			
Holzapfel, and Juergen Rauleder. Published by the American Institute of			
Aeronautics and Astronautics, Inc., with permission. All requests for			
copying and permission to reprint should be submitted to CCC at www.			
copyright.com; employ the eISSN 1533-3868 to initiate your request. See			
also AIAA Rights and Permissions https://aiaa.org/publications/publish-			
with-aiaa/rights-and-permissions/.			

^{*}Research Engineer, Daniel Guggenheim School of Aerospace Engineering; barzin.hosseini@gatech.edu. Member AIAA.

S	=	aerodynamic reference surface area (chosen as
		rotor disk area in this work), m ²
T	=	rotor thrust, N
U_p, U_T	=	perpendicular and tangential velocity compo-
ı		nents at the local rotor blade section, m/s
$oldsymbol{V}$	=	kinematic or aerodynamic velocity (depending

 v_i = kinematic of aerodynamic velocity (deponent on the index), m/s
= inflow velocity, m/s

 α = inflow state, rad α_A = aerodynamic angle of attack, rad β_A = aerodynamic angle of sideslip, rad

= rotor radius, m

 β = rotor flapping angle, rad λ_i = rotor induced inflow ratio

 λ_v = rotor inflow ratio due to the climb rate

 ω = angular rates, rad/s

 Ω = rotor rotational velocity, rad/s ϕ = rotor blade section inflow angle, rad Ψ = rotor blade azimuth angle, rad θ = rotor blade pitch angle, rad

 μ = rotor blade pitch angle, is μ = helicopter advance ratio

Subscripts

A = indicating the aerodynamic nature of a velocity or force

()_B = indicating that the vector in the brackets is given in the body-fixed frame

K = indicating the kinematic nature of a velocity or angular rate vector

R1/R2 = index indicating the nature of the force being the rotor 1 or 2

Superscripts

)^B = the coordinate frame (body-fixed) with respect to which the value in the bracket has been differentiated

1

[†]Research Engineer, Dynamic Systems and Control Branch, MS 308; jared.a.grauer@nasa.gov. Associate Fellow AIAA.

^{*}Department Head, Institute of Flight System Dynamics; florian. holzapfel@tum.de. Member AIAA.

[§]Assistant Professor, Daniel Guggenheim School of Aerospace Engineering; juergen.rauleder@gatech.edu. Associate Fellow AIAA.

G = indicating the acting point of a force or the reference point as the center of gravity

OB = of an angular rate: measured between the northeast-down frame O and the body fixed frame of the rotorcraft B

R1/R2 = index indicating the forces act at the rotor 1 or 2 coordinate frame origins

= derivative with respect to time

I. Introduction

HIGH-ORDER physics-based model was identified for a coaxial rotorcraft with a maximum takeoff weight (MTOW) of 600 kg based on flight test data and the blade element momentum theory (BEMT). The findings of this work supported a research project at the Technical University of Munich in which the CoAX 600 rotorcraft [1] was converted to the uncrewed aerial system (UAS) shown in Fig. 1 [2]. The CoAX 600 is a two-seater coaxial rotorcraft developed by edm aerotec GmbH. The rotorcraft obtained its type certificate under the ultralight class by the German Ultralight Association (*Deutscher Ultraleichtflugverband e.V.*). The simulation model developed in this study was used as a basis for the development of flight control functions, pilot training, and hardware-in-the-loop testing of avionics.

The model structure is nonlinear and consists of a rotor system coupled to a six-degree-of-freedom (6-DOF) rigid-body model. The model structure included unknown parameters relating mostly to the aerodynamics (forces and moments acting on the dynamic system) but also some of the mass properties of the rotorcraft, such as the moments of inertia. The unique features of the teetering rotor system were exploited for the simultaneous estimation of both the aerodynamic and mass property-related parameters, which is normally not feasible due to correlation issues. Maximum-Likelihood-based parameter estimation methods [3] were applied to estimate the unknown parameters in the time domain. A flight test campaign was performed on an instrumented CoAX 600 rotorcraft in its original crewed configuration to gather the flight data for parameter estimation. The instrumented crewed rotorcraft used for system identification can be seen in Fig. 4 and in the background of Fig. 2.

Two different common approaches have been used in the past for modeling rotorcraft. The first approach is the development of a rotorcraft simulation model based on first principles. The majority of these first-principle approaches model the forces and moments generated by the rotor system using BEMT [4,5]. The rotor system models vary in their level of fidelity and can include models of the different aspects of the rotor aeromechanics (e.g., flapping, lead-lag motion, and elasticity) and inflow dynamics. The rotor system model is coupled with a dynamic model of the fuselage and other aerodynamic surfaces, which can also vary based on the fidelity of the simulation model. Such physics-based models of specific rotorcraft are typically developed by using existing rotorcraft simulation



Fig. 1 CoAX 600 UAS.

and modeling frameworks such as FLIGHTLAB [6–8], RCAS [9], and CAMRAD II [10,11]. The parameters and underlying data in such models (e.g., geometry data and aerodynamic lookup tables) can be adjusted for a specific rotorcraft. If flight data are available, the model parameters can be adjusted such that the model outputs more accurately match flight data. However, the model development process is not primarily data-driven. Models of this kind are especially favorable if no or limited flight data are available during the modeling. Such models can be used in flight simulators, hardware-in-the-loop testing of avionics, and the development of initial flight control law structures.

In the second common approach for developing rotorcraft simulation models, flight data containing the pilot inputs and the aircraft response during dynamic maneuvers can be used to identify models of the rotorcraft via system identification techniques. Extensive work in this field has been done using frequency domain system identification methods, mostly using the frequency response methods described in Ref. [12] and the CIFER® (Comprehensive Identification from FrEquency Responses) toolbox [13] developed based on the methods of Ref. [12]. Linear models of the rotorcraft at the trim points where flight data are available can be identified using these methods. References [14–18] are a subset of numerous publications where the CIFER® toolbox has been used to identify dynamic systems of rotorcraft. Such linear models of the helicopter at different trim points can be stitched together as done in Refs. [12,19,20] to cover the full or an extended section of the flight envelope. Besides the helicopter system identification work in the frequency domain using CIFER®, important work on system identification of rotorcraft of different sizes has been done by the German Aerospace Center (Deutsches Zentrum für Luft- und Raumfahrt, DLR) in the time and frequency domains [21–24] and by other authors in Refs. [25–27].

A review of the cited literature reveals that most of the rotorcraft system identification work is performed in the frequency domain. This is in part because the rotorcraft dynamics are unstable in hover, which results in divergence problems when numerical optimization is applied to estimate the unknown system parameters in the time domain [28]. Furthermore, mostly simplified and linear model structures are used for parameter estimation. A physics-based nonlinear model structure of a helicopter involving a rotor system model (e.g., implemented based on BEMT) has so far not been used as a basis for rotorcraft parameter estimation. Such a model structure would rely on numerical methods to compute the external forces and moments on the rotorcraft at each time step. Therefore, embedding a physics-based model structure in the numerical optimization process, which requires repeated propagation of the model at each optimization iteration step, is a complex task and has not been performed for rotorcraft in the past. However, estimating parameters in a nonlinear physics-based model structure has been done for multiple fixed-wing aircraft in the past [29,30]. Such models offer a range of advantages when compared to linear models, such as their global nature over the flight envelope and the direct involvement of the flight physics and aerodynamics in the modeling process. The latter allows for easier interpretation of the parameter values and the observed model behavior, as well as a simpler comparison with wind tunnel data and aerodynamic prediction methods.

This paper demonstrates that the advantages of physics-based nonlinear models, as previously discussed, are applicable to rotorcraft as well. Furthermore, it is shown that the number of estimated parameters is smaller when physics-based rotorcraft model structures are used. The nonlinear model can be linearized at any trim point for system analysis and control design, in addition to being utilized in flight simulators in its original nonlinear form.

The paper starts with the description of the nonlinear physicsbased model structure in Sec. III and continues with the application of parameter estimation methods to determine the unknown parameter values in the system in Secs. IV and V. It follows with a

¹The use of trademarks or names of manufacturers in this report is for accurate reporting and does not constitute an official endorsement, either expressed or implied, of such products or manufacturers by NASA.

discussion of the identified model and some of the unique characteristics of the flight dynamics and aerodynamics of coaxial rotorcraft, which is a rotorcraft configuration not well studied by western countries. The model was linearized at different trim points and used to discuss the characteristics of the coaxial rotorcraft flight dynamics. The nonlinear and linearized models were utilized to develop the flight control laws for the rotorcraft (see Sec. VI). Finally, the influence of the developed flight control functions on the flight dynamics and handling qualities is discussed.

II. Nonlinear Model Structure

The CoAX 600 nonlinear model structure is developed around a 6-DOF rigid-body model, representing the fuselage and other aerodynamic surfaces but excluding the rotor blades. The equations of motion for a rigid body with its center of mass (CG) as reference point, and assuming a flat, nonrotating earth are the following [28]:

where $(V_K^G)_B^E$ is the kinematic (index K) velocity of the fuselage (rotorcraft excluding the rotor blades) at its center of gravity (G), $(\omega_k^{OB})_B$ is the rotational velocity, $(I^G)_{BB}$ is the inertia tensor, and m is the mass of the rotorcraft fuselage. Bold symbols in the equations represent vectors and matrices. The index B indicates that vectors are denoted in the rotorcraft body-fixed frame. The coordinate frames used in this work are described in Sec. III.A. $\sum (F^G)_B$ and $\sum (M^G)_B$ are the sum of the external forces and moments acting on the fuselage at its center of gravity as denoted by the superscript G. In this study, they are the sum of the aerodynamic forces directly acting on the rotorcraft body $(F_A^G)_B$, $(M_A^G)_B$, and the forces and moments exerted by the rotor system $(F_B^G)_B$, $(M_B^G)_B$

$$\sum (F^{G})_{B} = (F_{A}^{G})_{B} + (F_{R}^{G})_{B}$$

$$\sum (M^{G})_{R} = (M_{A}^{G})_{R} + (M_{R}^{G})_{R}$$
(2)

The superscripts of the velocity and the acceleration in Eq. (1) indicate the coordinate frames, which were used as the reference for derivation with respect to time. The superscript E in $(V_B^G)_B^E$ indicates that the position was differentiated with respect to time in the Earthcentered, Earth-fixed coordinate frame to obtain the velocity vector,

and EB in the acceleration $(\dot{V}_K^G)_B^{EB}$ indicates that the mentioned velocity was differentiated in the body-fixed frame. The external forces and moments acting on the fuselage were computed separately via a static aerodynamic model for the aerodynamic forces acting directly on the fuselage and the rotor system. The following subsections give an overview of the computation of these forces and moments

A. Coordinate Frames

Multiple coordinate frames were used to compute the rotor and fuselage forces and moments and for setting up the equations of motion. Figure 2 gives an overview of the coordinate frames defined on the helicopter that were used throughout this work. The bodyfixed frame is centered at the reference point of the rotorcraft, which was selected to be the center of mass in this study, as is the standard for flight dynamics. The x_B axis points out the nose of the helicopter and the z_B is parallel to the rotor shaft pointing downward. Note that y_B points toward right such that a right-hand coordinate frame is formed. The rotor forces and moments are first computed in the rotor coordinate frames denoted by index R1 for the lower rotor and R2 for the upper rotor. Each rotor coordinate is centered at the teeter joint of the respective rotor. In the absence of rotor flapping, x_{Ri} $(i \in 1, 2)$ axes are parallel to x_B pointing backward, z_{Ri} is parallel to the rotor shaft, pointing upward, and y_{Ri} are parallel to the bodyfixed y_B and point to the same direction. When the rotor flapping angle is nonzero, the rotor coordinate frame tilts together with the rotor, such that the tip-path-plane of each rotor coincides with the respective plane spanned by the x_{R_i} and y_{R_i} axes of the rotor coordinate frames. Each blade also has its own coordinate frame, in which the local forces and moments of the blade element are computed. They are denoted by the index bij, where $i \in 1,2$ specifies the rotor and $j \in 1, 2$ specifies the blade on the rotor. The z_{bij} is parallel to z_R , also pointing upward; x_{bij} is tangential to the in-plane motion of the blade and points in the same direction; y_{bij} forms a right-hand coordinate frame with x_{bij} and z_{bij} . The center of this coordinate frame can be moved across the blade. However, if not stated otherwise, the rotating blade coordinate frames are also centered at the teeter joint.

B. Rotor System Model

The rotor system forces are computed via a discrete implementation of the BEMT as described in Ref. [4]. In this setup, each blade is divided into discrete sections along its radius. The forces and moments at each of the radial sections can be computed using the aerodynamic coefficients of the two-dimensional blade airfoil

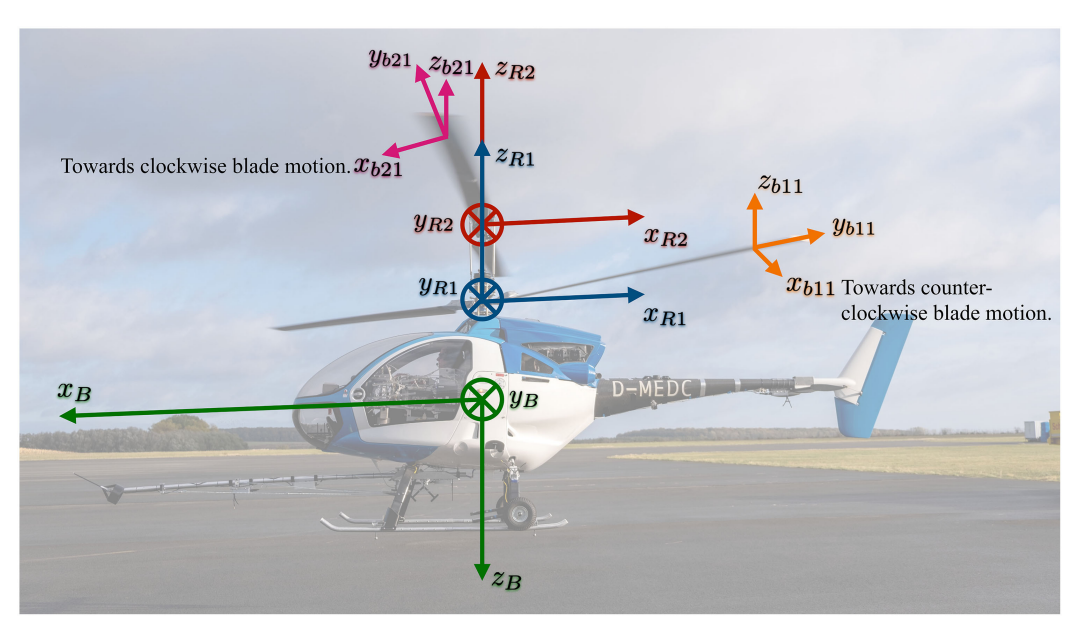


Fig. 2 The body-fixed, rotor, and blade coordinate frames on the helicopter.

 $(C_{R_l}, C_{R_d}, \dots)$ at each of the respective radial sections. The lift and drag coefficients are modeled as

$$C_{R_l} = C_{R_{l_0}} + \alpha_A C_{R_{l_\alpha}}, \quad C_{R_d} = C_{R_{d_0}} + \alpha_A C_{R_{d_\alpha}} + \alpha^2 C_{R_{d_2}}$$
 (3)

where $\alpha_A = \theta - \phi$ is the local angle of attack of the blade element. It is influenced by the local blade pitch angle θ and the local inflow angle ϕ outlined in Eq. (5). $C_{R_{I_0}}$, $C_{R_{I_a}}$, $C_{R_{J_0}}$, $C_{R_{J_a}}$, and $C_{R_{J_a}}$ are among the unknown aerodynamic parameters that are estimated based on flight data. In this study, only the vertical and horizontal forces at each blade section were considered, and the local pitch moment was not explicitly modeled. This simplification will affect other model parameter values, much like other unmodeled phenomena discussed in Sec. III.C. The vertical dF_z and horizontal dF_x force increments in the blade coordinate frame were calculated as follows [4]:

$$dF_z = dL\cos\phi - dD\sin\phi \approx dL = \frac{1}{2}\rho cC_{R_{l_a}}(\theta U_T^2 - U_P U_T)dy$$
(4a)

$$dF_x = dL \sin \phi + dD \cos \phi \approx \phi dL + dD$$

$$= \frac{1}{2} \rho c C_{R_{l_a}} \left(\theta U_P U_T - U_P^2 + \frac{C_{R_d}}{C_{R_{l_a}}} U_T^2 \right) dy$$
 (4b)

where dL and dD are the lift and drag increments, dy is the incremental blade section length, c is the blade chord length, and U_P and U_T are perpendicular and tangential local blade velocities, respectively. Note that the small-angle approximation was applied in the above equation since $U_T \gg U_P$. ϕ is the relative inflow angle:

$$\phi = \tan^{-1} \left(U_P / U_T \right) \approx U_P / U_T \tag{5}$$

The local blade pitch angle θ was computed as follows:

$$\theta = \begin{cases} \theta_0 + \theta_{\text{twist}}(r) + \theta_{\text{col}} + c_\beta \theta_c \cos \Psi + c_\beta \theta_s \sin \Psi & \text{Lower Rotor} \\ \theta_0 + \theta_{\text{twist}}(r) + \theta_{\text{col}} - c_\beta \theta_c \cos \Psi - c_\beta \theta_s \sin \Psi + \theta_{\text{yaw}} & \text{Upper Rotor} \end{cases}$$
(6)

Here, $\theta_{\rm col}$, θ_c and θ_s , and $\theta_{\rm yaw}$ represent the collective, cyclic, and yaw commands; $\theta_{\rm twist}$ describes the effect of the linear twist; and $\theta_0 = (C_{R_{l_0}}/C_{R_{l_a}})$ accounts for the blade lift coefficient at zero angle of attack $C_{R_{l_0}}$. It should be noted that the yaw input $\theta_{\rm yaw}$ only affects the upper rotor on the CoAX 600, as in Eq. (6). This input affects the torque of the upper rotor to induce a net yaw moment on the fuselage. The parameter c_{β} scales the cyclic pilot inputs since it was observed that the effective cyclic input of the local blade pitch angle was smaller than the estimated inputs, according to the measurements at the swashplate, as described in Sec. V.C. The local blade velocities at each blade section were computed for the lower rotor as follows:

$$U_{T_{p_1}}(y, \Psi) = \Omega y + V_A \cos \alpha_A \sin \Psi \tag{7}$$

$$U_P(y, \Psi) = (\lambda_v + \lambda_i)\Omega R + y\dot{\beta}(\Psi) + \mu\Omega R\beta(\Psi)\cos(\Psi) \quad (8)$$

The tangential rotor blade velocity on the upper rotor varies because of the reversed rotation direction:

$$U_{T_{R2}}(y, \Psi) = \Omega y - V_A \cos \alpha_A \sin \Psi \tag{9}$$

The local aerodynamic velocity of each blade section depends on the azimuth angle of each blade Ψ and the radial position of the blade section y. Furthermore, V_A is the total aerodynamic velocity, α the aerodynamic angle of attack, and Ω the rotational speed of the rotor. The nondimensional vertical velocity λ_v and the advance ratio μ were computed as

$$\lambda_v = \frac{V_A \sin \alpha_A}{\Omega R}, \quad \mu = \frac{V_A \cos \alpha_A}{\Omega R} \tag{10}$$

The induced inflow of the rotor $\lambda_i = (v_i/\Omega R)$ at each blade section was modeled using a finite state inflow model for coaxial helicopters that was developed in Ref. [31] and implemented in Ref. [32]. The inflow model is reviewed in Sec. III.B.1 of this paper.

Each rotor, which contains two blades, was modeled as a rigid body. The flapping motion of these blades was modeled using the following differential equation [5]:

$$\frac{1}{\Omega^2}\ddot{\beta} + \lambda_{\beta}^2 \beta = \frac{2}{\Omega} (p\cos\Psi - q\sin\Psi) + \frac{1}{I_{\beta}\Omega^2} M_{\beta}$$
 (11)

where M_{β} is the rotor hinge moment around the flapping hinge and λ_{β} represents the overall torsion spring stiffness of the flapping hinge, which is $\lambda_{\beta}=1$ for a teetering rotor with no flapping springs [5]. I_{β} is the moment of inertia of both blades around the flapping hinge. It is assumed that flapping motion is described by the following equation:

$$\beta(t) = \beta_c(t)\cos(\Omega t) + \beta_s(t)\sin(\Omega t) \tag{12}$$

which reformulates the time-periodic differential equation of Eq. (11) as two different time-invariant systems.

The first and second time derivatives of the above equation were calculated and substituted into Eq. (11). The comparison of similar terms and simplification for a teetering rotor results in the following coupled differential equations:

$$\ddot{\beta}_c = -2\dot{\beta}_s \Omega + 2\Omega p + \frac{c_{\beta_c}}{I_\beta} M_{\beta_c} \tag{13}$$

$$\ddot{\beta}_s = 2\dot{\beta}_c \Omega - 2\Omega q + \frac{c_{\beta_s}}{I_B} M_{\beta_s}$$
 (14)

where M_{β_c} and M_{β_s} are the cosine and sine terms of the periodic flapping moment $M_{\beta}=M_{\beta_c}\cos(\Omega t)+M_{\beta_s}\sin(\Omega t)$. The parameters c_{β_c} and c_{β_s} are empirical correction factors and represent the loss effects and nonlinear load distribution over the rotor blade that result in a different flapping hinge moment, as compared with the ideal values computed via BEMT. They also allow for considering the inaccuracies in the CAD-based value of the rotor blades moment of inertia around the flapping hinge. The mentioned parameters will be treated as unknowns and will be estimated in the system identification process. Note that the small effects of the rotor shaft angular accelerations were neglected in the flapping equations of motion, as suggested in Ref. [5].

The forces of each rotor blade element, computed by Eq. (4a), are summed in Eq. (15) to determine the overall loads of each rotor in its blade coordinate frame. The indices b1 and b2 indicate the notation of the vectors in the blade coordinate frames of rotors 1 and 2 (cf. Fig. 2). The forces of each rotor (indices R1 and R2) act on the origin of each rotor coordinate frame (superscripts R1 and R2), i.e., at the rotor shaft with an offset to the rotorcraft CG.

$$(\boldsymbol{F}_{R1}^{R1})_{b1} = \begin{bmatrix} \sum_{i=1}^{N_s} (dF_{x_{R1b1}})_i - \sum_{i=1}^{N_s} (dF_{x_{R1b2}})_i \\ 0 \\ \sum_{i=1}^{N_s} (dF_{z_{R1b1}})_i + \sum_{i=1}^{N_s} (dF_{z_{R1b2}})_i \end{bmatrix}$$
 (15)

$$(\mathbf{F}_{R2}^{R2})_{b2} = \begin{bmatrix} -\sum_{i=1}^{N_s} (dF_{x_{R2b1}})_i + \sum_{i=1}^{N_s} (dF_{x_{R2b2}})_i \\ 0 \\ \sum_{i=1}^{N_s} (dF_{z_{R2b1}})_i + \sum_{i=1}^{N_s} (dF_{z_{R2b2}})_i \end{bmatrix}$$
 (16)

with N_s being the number of blade element sections on each blade, selected as 10 in this study. Reference [33] shows that 10 sections is sufficient to adequately compute the rotor forces and moments for

flight dynamics purposes. In the next step, the rotor forces are transformed into the rotor coordinate frame

$$(F_{R1}^{R1})_{R1} = \begin{bmatrix} \left(\sum_{i=1}^{N_s} \left(dF_{x_{R1b1}}\right)_i - \sum_{i=1}^{N_s} \left(dF_{x_{R1b2}}\right)_i\right) \cos(\psi) \\ \left(\sum_{i=1}^{N_s} \left(dF_{x_{R1b1}}\right)_i - \sum_{i=1}^{N_s} \left(dF_{x_{R1b2}}\right)_i\right) \sin(\psi) \\ \sum_{i=1}^{N_s} \left(dF_{z_{R1b1}}\right)_i + \sum_{i=1}^{N_s} \left(dF_{z_{R1b2}}\right)_i \end{aligned}$$

$$(17)$$

$$(F_{R2}^{R2})_{R2} = \begin{bmatrix} \left(-\sum_{i=1}^{N_s} \left(dF_{x_{R2b1}} \right)_i + \sum_{i=1}^{N_s} \left(dF_{x_{R2b2}} \right)_i \right) \cos(\psi) \\ \left(-\sum_{i=1}^{N_s} \left(dF_{x_{R2b1}} \right)_i + \sum_{i=1}^{N_s} \left(dF_{x_{R2b2}} \right)_i \right) \\ \sin(\psi) \sum_{i=1}^{N_s} \left(dF_{z_{R2b1}} \right)_i + \sum_{i=1}^{N_s} \left(dF_{z_{R2b2}} \right)_i \end{bmatrix}$$

$$(18)$$

The first two elements of the rotor force vectors of Eq. (17) are the in-plane components of the rotor force, and the third element is the rotor thrust T. The superscripts R1 and R2 indicate that the forces are exerted at the lower and upper rotor positions, respectively. Note that Eq. (17) computes the rotor forces as a function of the blade azimuth angle ψ . In this study, a full rotor rotation is computed at each simulation time step, and the rotor forces and moments are averaged over a full revolution. For this purpose, the rotor disk was split into 20 azimuthal sections (i.e., angular increments of 18 deg). These are reasonable approximations because the rotor rotational velocity is significantly faster than the rotorcraft dynamics. This approach was adopted to simplify the problem structure for parameter estimation. The yaw moment (torque) that each rotor exerts on the fuselage can be computed based on the in-plane force of the blade sections from Eq. (15) as follows:

$$(N_{R1}^{R1})_{b1,z} = (N_{R1}^{R1})_{R1,z} = -\sum_{i=1}^{N_s} y_i (dF_{x_{R1b1}})_i - \sum_{i=1}^{N_s} y_i (dF_{x_{R1b2}})_i$$
 (19)

$$(N_{R2}^{R2})_{b2,z} = (N_{R2}^{R2})_{R2,z} = \sum_{i=1}^{N_s} y_i (dF_{x_{R2b1}})_i + \sum_{i=1}^{N_s} y_i (dF_{x_{R2b2}})_i$$
 (20)

where y_i is the distance of the center of the respective blade section from the rotor hub. The resulting yaw moment of the full rotor system, consisting of the upper and lower rotors

$$\left(N_{R1/2}^{R1/2}\right)_{R.7} = -\left(N_{R1/2}^{R1/2}\right)_{R1/2.7} = -\left(N_{R1}^{R1}\right)_{R1} - \left(N_{R2}^{R2}\right)_{R2} \tag{21}$$

is zero at hover and otherwise used to control the yaw motion of the rotorcraft by changing the collective pitch of the upper rotor θ_{yaw} [see Eq. (6)].

The pitch and roll moments directly acting on the rotorcraft from the rotors were neglected in light of the teetering rotor system. Because the rotors are offset from the CG, the teetering rotor configuration can exert pitch and roll control moments on the airframe. The direction of the thrust and drag vector of each rotor can be controlled via the flapping motion. The rotor forces of Eq. (17) are projected onto the rotorcraft body-fixed frame coordinate directions. The components of the rotor forces in the body frame of the rotorcraft $(F_{R1/2}^{R1/2})_B$ become

$$\left(\boldsymbol{F}_{R1/2}^{R1/2} \right)_{x,B} = \left(\boldsymbol{F}_{R1/2}^{R1/2} \right)_{z,R1/2} \sin \beta_{R1/2_c} \cos \beta_{R1/2_s}$$

$$- \left(\boldsymbol{F}_{R1/2}^{R1/2} \right)_{x,R1/2} \cos \beta_{R1/2_c}$$
 (22)

$$(\boldsymbol{F}_{R1/2}^{R1/2})_{y,B} = -(\boldsymbol{F}_{R1/2}^{R1/2})_{z,R1/2} \sin \beta_{R1/2_s} \cos \beta_{R1/2_c} -(\boldsymbol{F}_{R1/2}^{R1/2})_{y,R1/2} \cos \beta_{R1/2_c}$$
(23)

$$\left(\boldsymbol{F}_{R1/2}^{R1/2}\right)_{z,B} = -\left(\boldsymbol{F}_{R1/2}^{R1/2}\right)_{z,R1/2} \cos \beta_{R1/2_c} \tag{24}$$

The above rotor forces and the rotor yaw moment (torque) are resolved to the CG of the helicopter. This results in the rotor forces and moments, which are used in the equations of motion [Eq. (1)].

$$(F_{R1/2}^G)_B = (F_{R1/2}^{R1/2})_B$$
 (25)

$$(\boldsymbol{M}_{R1/2}^G)_B = (\boldsymbol{r}^{GR1/2})_B \times (\boldsymbol{F}_{R1/2}^{R1/2})_B + \left[0, 0, \left(N_{R1/2}^{R1/2}\right)_{B,z}\right]^T$$
 (26)

where $(\mathbf{r}^{GR1/2})_B$ is the position of each rotor with respect to the center of gravity G. The sum of the forces $(\mathbf{F}_R^G)_B$ and moments $(\mathbf{M}_R^G)_B$ of rotors 1 and 2 from Eq. (25) are then inserted in Eq. (2) to be used in the equations of motion [Eq. (1)].

1. Finite State Dynamic Inflow Model

The finite state dynamic inflow model was derived from fundamental aerodynamic principles such as the momentum and continuity equations under certain assumptions. The detailed derivation can be found in Refs. [31,32]. This approach for modeling the rotor inflow is also called the *Pressure Potential Superposition Inflow Model* (PPSIM). The inflow model can be stated as follows:

$$\begin{bmatrix} M_{11} & M_{12} \\ M_{21} & M_{22} \end{bmatrix} \begin{bmatrix} \dot{\boldsymbol{\alpha}}_1 \\ \dot{\boldsymbol{\alpha}}_2 \end{bmatrix} + \begin{bmatrix} \boldsymbol{V}_{m_1} & 0 \\ 0 & \boldsymbol{V}_{m_2} \end{bmatrix} \begin{bmatrix} L_{11} & L_{12} \\ L_{21} & L_{22} \end{bmatrix}^{-1} \begin{bmatrix} \boldsymbol{\alpha}_1 \\ \boldsymbol{\alpha}_2 \end{bmatrix}$$

$$= \frac{1}{2} \begin{bmatrix} \boldsymbol{\tau}_1 \\ \boldsymbol{\tau}_2 \end{bmatrix}$$
(27)

The inflow states α_i and their time derivatives $\dot{\alpha}_i$ for each rotor consist of a uniform part and a defined number of cosine and sine terms. In this study, only the uniform part and the first-order harmonic terms were considered, as it is common for rotorcraft flight dynamics models because the higher-order harmonics do not significantly contribute [34]. The indices "1" and "2" represent the lower and upper rotor disks of the coaxial rotor system, respectively. Furthermore, the inflow states describe the rotor inflow along the z_{Ri} axis of the rotor coordinate frame. The matrices M and L are often referred to as the inflow mass and gain matrices, which depend on the inflow velocity, the advance ratio, and the wake skew angle [5,34]. The values for the M- and L-matrices were computed in advance for multiple forward flight velocities and are stored in lookup tables. The matrix elements are interpolated between the discrete advance ratios at which the matrices were computed. The matrices also account for the interaction of the rotors with each other. Primarily, the inflow velocity of the lower rotor is significantly affected by the induced inflow velocity of the upper rotor, as the lower rotor operates in the downwash of the upper rotor.

The τ_i vectors for the lower and upper rotor $i \in \{1,2\}$ represent the external forces and moments. In the special case of considering only the first harmonics, the elements of $\tau_i = [\tau_i^{0c}, \tau_i^{1c}, \tau_i^{1s}]$ for each rotor can be written down as

$$\tau_i^{0c} = \frac{\sqrt{3}}{4\pi\rho\Omega^2 R^4} T_i \tag{28}$$

$$\boldsymbol{\tau}_i^{1c} = \sqrt{\frac{15}{8}} \frac{1}{\pi \rho \Omega^2 R^5} M_{\beta_i} \cos \Psi_i \tag{29}$$

$$\tau_i^{1s} = \sqrt{\frac{15}{8}} \frac{1}{\pi \rho \Omega^2 R^5} M_{\beta_i} \sin \Psi_i \tag{30}$$

by solving the original integrals for the generic case from Refs. [31,32]. The rotor hinge moment M_{β} and thrust T are computed using BEMT, as described above. The mass flow parameters

 V_{m_i} for the lower and upper rotors $(i \in \{1, 2\})$ can be computed as follows:

$$V_{m_i} = \operatorname{diag}(V_{T_i}, V_i, \dots, V_i) \tag{31}$$

$$V_i = \frac{\mu^2 + (\lambda_{m_i} + \lambda_i)\lambda_i}{V_{T_i}}$$
 (32)

$$V_{T_i} = \sqrt{\mu^2 + \lambda_i^2} \tag{33}$$

$$\lambda_i = \lambda_{m_i} + \lambda_v \tag{34}$$

where λ_{m_i} is the momentum theory equivalent inflow of each rotor and can be computed based on the uniform part of the inflow states (i.e., the first element in the inflow state vectors α_{i_1}) as described in Refs. [31,32]:

$$\lambda_{m_i} = \sqrt{3}\alpha_{i_1} \tag{35}$$

C. Fuselage Static Aerodynamic Model

The forces and moments acting on the fuselage were modeled in a similar way to the fixed-wing aircraft, as described in Ref. [28]. The aerodynamic forces acting on the fuselage are modeled as

$$(F_A^G)_B = \mathbf{M}_{BA}\bar{q}S \begin{bmatrix} -C_D \\ C_Q \\ -C_L \end{bmatrix}$$
(36)

where \bar{q} is the dynamic pressure; S is chosen as the rotor disk area; C_L , C_D , and C_Q are the lift, drag, and side force coefficients, respectively, and

$$\mathbf{M}_{BA} = \begin{bmatrix} \cos \alpha_A \cos \beta_A & -\cos \alpha_A \sin \beta_A & -\sin \alpha_A \\ \sin \beta_A & \cos \beta_A & 0 \\ \sin \alpha_A \cos \beta_A & -\sin \alpha_A \sin \beta_A & \cos \beta_A \end{bmatrix}$$
(37)

is the transformation matrix from the aerodynamic coordinate frame to the body-fixed frame. The aerodynamic moments acting on the fuselage, with the CG as a reference point, are computed as follows:

where the characteristic length D_R is the rotor diameter. The parameters C_l , C_m , and C_n are roll, pitch, and yaw moment coefficients. The nondimensional aerodynamic parameters involved in the equations above are a function of the flight condition [28] and the pilot rudder input ζ , which is a linear function of the rotor yaw input $\zeta = c\theta_{\rm yaw}$. This dependency is modeled as follows:

$$C_L = C_{L_0} + C_{L_{\alpha}} \alpha_A \tag{39}$$

$$C_D = C_{D_0} + C_{D_{a_1}} \alpha_A \tag{40}$$

$$C_{Q} = C_{Q_{0}} + C_{Q_{\beta_{A}}}\beta_{A} + C_{Q_{r}}\frac{rD_{R}}{2V_{A}} + C_{Q_{\zeta}}\zeta$$
(41)

$$C_{l} = C_{l_{0}} + C_{l_{\beta_{A}}} \beta_{A} + C_{l_{p}} \frac{pD_{R}}{2V_{A}} + C_{l_{r}} \frac{rD_{R}}{2V_{A}} + C_{l_{\zeta}} \zeta$$
 (42)

$$C_m = C_{m_0} + C_{m_{\alpha_A}} \alpha_A + C_{m_q} \frac{qR}{2V_A}$$
 (43)

$$C_n = C_{n_0} + C_{n_{\beta_A}} \beta_A + C_{n_r} \frac{rD_R}{2V_A} + C_{n_p} \frac{qD_R}{2V_A} + C_{n_{\zeta}} \zeta$$
 (44)

The model structure above was chosen based on previous experience and was validated in the system identification process. The model structure allows for adding further terms. In the above equations, V_A is the absolute value of the aerodynamic velocity. Any unmodeled phenomena and interaction between the rotor forces and moments will be lumped into the numerical values for the rotor and fuselage aerodynamic parameters as they are not accounted for explicitly.

D. Integrated Simulation Model

The different subsystems of the CoAX 600 rotorcraft simulation model and their interaction with each other are shown in Fig. 3. The environment was modeled according to the U.S. standard atmosphere [35]. The unsteady behavior between the different layers of the atmosphere was modeled via a continuous approximation using the hyperbolic tangent tanh [36], which is commonly used as a

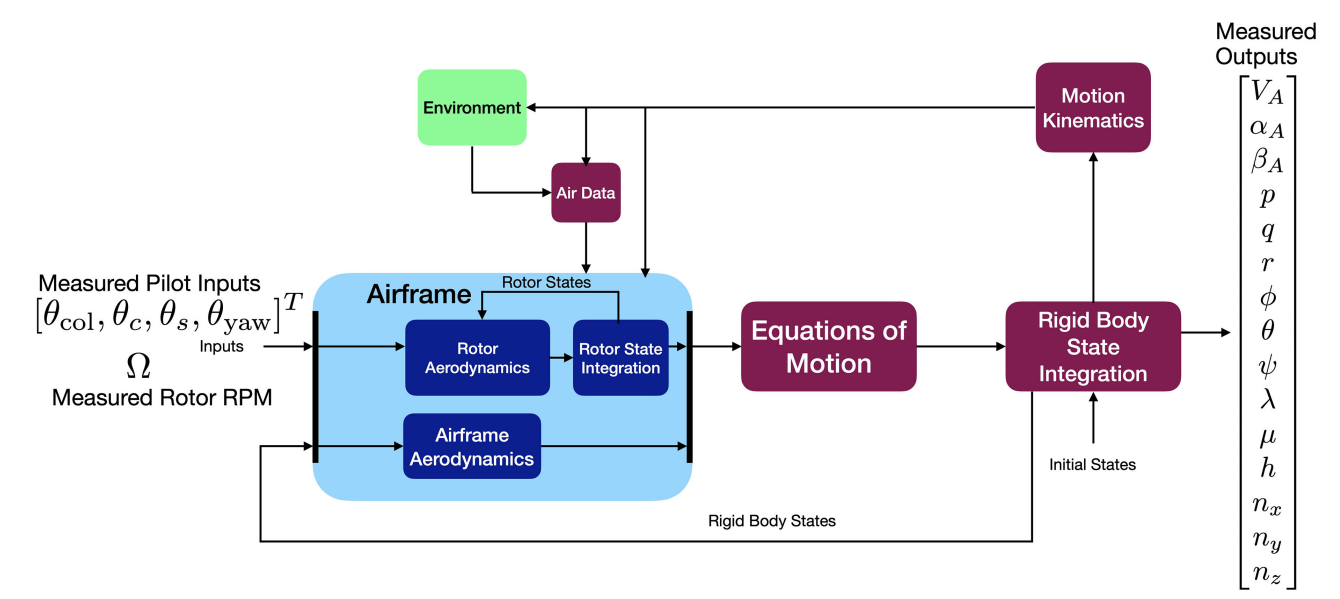


Fig. 3 Overview of the model structure for the CoAX 600 coaxial helicopter.

differentiable switching function. The full simulation model has the following inputs, states, and outputs:

$$\boldsymbol{u} = [\theta_{\text{col}}, \theta_c, \theta_s, \theta_{\text{yaw}}]^T \tag{45}$$

$$\mathbf{x} = [u_{K}, v_{K}, w_{K}, p, q, r, \phi, \theta, \psi, \lambda, \mu, h, \beta_{R1_{c}}, \dot{\beta}_{R1_{c}}, \beta_{R1_{c}}, \dot{\beta}_{R1_{c}}, \beta_{R2_{c}}, \dot{\beta}_{R2_{c}}, \beta_{R2_{c}}, \dot{\beta}_{R2_{c}}, \alpha_{R1_{c}}, \alpha_{R1_{c}}, \alpha_{R1_{c}}, \alpha_{R2_{c}}, \alpha_{R2_{c}}, \alpha_{R2_{c}}]^{T}$$
(46)

$$\mathbf{y} = [V_A, \alpha_A, \beta_A, p, q, r, \phi, \theta, \psi, \lambda, \mu, h, n_x, n_y, n_z]^T \tag{47}$$

where n_x , n_y , and n_z are the load factors in the x_B , y_B , and z_B direction of the body-fixed frame at the position of the inertial measurement unit (IMU) installed onboard. The correction of the accelerations to account for the offset between the CG and the IMU, as well as the computation of the load factors from rigid-body accelerations (e.g., accounting for Earth gravity), is discussed in Ref. [37]. The resulting model structure of the helicopter, described by the above equations, takes the following form:

$$\dot{\mathbf{x}} = f(\mathbf{x}, \mathbf{u}, \boldsymbol{\theta}) \tag{48}$$

$$\mathbf{v} = \mathbf{g}(\mathbf{x}, \mathbf{u}, \boldsymbol{\theta}) \tag{49}$$

where θ is the vector of the model parameters. This is a system of nonlinear ordinary differential equations describing the rotorcraft dynamics over its flight envelope. The original time-periodic differential equation of the flapping motion [Eq. (11)] was replaced with the ordinary differential equations of Eq. (13) and Eq. (14) such that Eq. (48) does not involve any time-periodic components.

III. Parameter Estimation Method

The unknown parameters in the helicopter model structure were estimated in the time domain using an optimal control-based implementation of the Maximum-Likelihood method with the outputerror formulation. The details of the Maximum-Likelihood parameter estimation can be found in Refs. [28,38], and for a summary of the specific implementation used in this study, Refs. [3,39] can be consulted. The optimal control and parameter estimation toolbox that was used in this study, falcon.m, is released by the Institute of Flight System Dynamics of Technical University of Munich** and is free for noncommercial use.

The Maximum-Likelihood method minimizes the cost function

$$J(\boldsymbol{\theta}) = \frac{1}{2} \sum_{i=1}^{N} [\boldsymbol{z}(t_i) - \boldsymbol{y}(t_i, \boldsymbol{\theta})]^T \boldsymbol{R}^{-1} [\boldsymbol{z}(t_i) - \boldsymbol{y}(t_i, \boldsymbol{\theta})] + \frac{N}{2} \ln (|\boldsymbol{R}|)$$
(50)

over N time samples, where z is the measurement vector, y the output vector, and θ the parameter vector. The matrix R is the measurement noise covariance matrix, which is also unknown and estimated alongside the model parameters in a two-step relaxation strategy [28]. An update for the optimal noise covariance matrix R, given a fixed set of model parameters, is computed by solving the equation $(\partial J/\partial R) = 0$ for R. This can be done analytically and results in the following closed-form update for the noise covariance matrix R after each parameter update step during the numerical optimization of the cost function [Eq. (50)]:

$$\hat{\mathbf{R}} = \frac{1}{N} \sum_{i=1}^{N} [\mathbf{z}(t_i) - \mathbf{y}(t_i, \boldsymbol{\theta})] [\mathbf{z}(t_i) - \mathbf{y}(t_i, \boldsymbol{\theta})]^T$$
 (51)

Application of the time-domain parameter estimation methods to unstable dynamic systems is known to be associated with convergence issues and therefore challenging [28,38]. This is part

of the reason that frequency-domain methods are more widely used for helicopter parameter estimation [12]. However, the optimal control-based implementation of the parameter estimation method [39] used in this study alleviates this issue and increases the convergence radius. The mentioned implementation replaces the integration of the dynamic system over time with the full discretization of the trajectory and enforces the system dynamics in Eq. (48) via optimization constraints. The optimization constraints include system dynamics and additional constraints defined by the user (e.g., parameter constraints).

Note that falcon.m also computes an estimate for the parameter covariance matrix, which can be used by the user to assess the accuracy of the estimated parameters and is helpful in the context of model validation. This is determined by falcon.m based on the Hessian of the cost function of Eq. (50). The diagonal elements of the parameter covariance matrix are the parameter variances σ_{θ}^2 used to compute the parameter standard error σ_{θ} . The off-diagonal elements of the covariance matrix are used to compute the correlation indices of each parameter pair. The correlation index for each of the two parameters in the model is calculated as follows [28]:

$$\operatorname{corr}(\theta_i, \theta_j) = [\rho_{ij}] = \frac{\operatorname{cov}(\theta_i, \theta_j)}{\sigma(\theta_i)\sigma(\theta_i)}$$
 (52)

where $\sigma(\theta_i)$ and $\sigma(\theta_j)$ are the standard deviations of the parameters θ_i and θ_j . The correlation indices can be collected in a matrix ρ , calculated as

$$\rho = \begin{bmatrix} \frac{1}{\sigma(\theta_1)} & \dots & 0 \\ \vdots & \ddots & \vdots \\ 0 & \dots & \frac{1}{\sigma(\theta_{n_n})} \end{bmatrix} \operatorname{cov}(\boldsymbol{\theta}) \begin{bmatrix} \frac{1}{\sigma(\theta_1)} & \dots & 0 \\ \vdots & \ddots & \vdots \\ 0 & \dots & \frac{1}{\sigma(\theta_{n_n})} \end{bmatrix}$$
(53)

with n_p being the number of the parameters in the system. Some of the noise dealt with in this study is colored and contains serial correlations. In this case, the corrections suggested in Ref. [28] should be applied when interpreting the computed estimates for the parameter uncertainties in this study.

IV. Parameter Estimation Results

The flight data recorded during the test campaign of 2021 in Obermehler, Germany [40] (Fig. 4), were used for estimating the rotorcraft model parameters in this study. These data were collected in hover and forward flight velocities (indicated airspeeds) of approximately 60, 80, and 120 km/hr. The flown maneuvers were a collection of multistep signals designed based on an *a priori* model of the rotorcraft, as described in Ref. [38]. Such methods rely on linear system analysis to effectively select the step sizes in multistep signals such as doublets and 3-2-1-1s and were manually executed by a test pilot. The test data were recorded with a sampling



Fig. 4 Instrumented CoAX 600 during manned flight tests.

^{**}Data available online at https://www.fsd.ed.tum.de/software/falcon-m/.

rate of 50 Hz. The inertial measurement unit was equipped with an internal anti-aliasing filter. No additional filtering was applied to the flight data.

A. CoAX 600

The two blades of each rotor of the CoAX 600 rotorcraft are connected to each other (modeled as the rigid body) and are mounted on the rotor shaft with a teetering mechanism. The rotor system is powered by a single UL Power 390iS power plant, and a governor keeps the motor RPM constant. The helicopter does not have a tail rotor because the counter-rotating rotors provide the torque balance.

In hover, the pilot controls the yaw motion of the helicopter by adjusting the collective pitch of the upper rotor via the pedals. This adjustment causes a torque imbalance between the rotors, generating a net yaw moment that acts on the fuselage. Additionally, the vertical stabilizer houses a rudder ζ (also controlled by the pedals) that assists the rotor system to generate additional yaw moment during forward flight. Some of the important design parameters of the helicopter are provided in Table 1.

The position of the CG has also been estimated using flight data supported by the study of Ref. [41]. The CG position can vary slightly between the maneuvers. This has been estimated alongside the parameters discussed in Sec. V.C for each maneuver. The values of the inertia matrix were also estimated using flight data in hover by exploiting the characteristics of the teetering rotor system. This process is described in Sec. V.C. The mass of the rotor blades is included in the calculation of the overall mass of the helicopter m and the CG position. However, the blade contributions are excluded from the computation of the helicopter roll and pitch moments of inertia. The blade inertia is explicitly accounted for in the flapping equations of motion [Eqs. (13) and (14)].

B. Instrumentation and Measurement of Flight Parameters

The rotorcraft was equipped with a wide array of aerospace-grade sensors for the flight tests. The linear accelerometer outputs, angular rates, and attitude angles were measured by an Archangel Systems attitude heading reference system (AHRS) AHR150A [42] with an integrated air data computer. Three additional remote inertial measurement units were used to validate the AHRS data (cf. Fig. 5a). An air data probe, which is gimbal-mounted on a boom extending out of the rotor radius to avoid the influence of the rotor downwash, was used to measure the aerodynamic velocity and the angles of attack α_A and sideslip β_A (Figs. 2 and 5b).

A NexNav GPS SBAS sensor unit [43] was used for the primary

A NexNav GPS SBAS sensor unit [43] was used for the primary measurement of the rotorcraft position and the kinematic velocity. The three experimental remote IMUs also had integrated GPS receivers. The antennas of the four independent GPS receivers were



a) AHRS and IMU



b) Air data boom

Fig. 5 Instrumentation onboard the helicopter.

positioned at front and aft locations of the helicopter to allow for the computation of the GPS heading.

Tension cable potentiometers (see Fig. 6) were used to measure the position of the three pushrods of the swashplate of the lower rotor. The pushrod measurements were translated to collective and cyclic pitch angles of Eq. (6) via a kinematics model of the rotor mechanical control system. This kinematic model was developed using measurements of the nonrotating rotor on the ground. For this purpose, the rotor blade pitch angles were measured manually at different azimuth angles for both the lower and upper rotors for multiple combinations of the collective lever position and stick forward and aft positions. The blade pitch angles were measured manually using a handheld inclinometer that could be magnetically attached to each blade. The three swashplate pushrod potentiometer readings were also recorded at each test point.

A linear mapping of the following form has been identified based on the measurement data described above to determine the collective and cyclic blade pitch angles of Eq. (6):

Table 1 Configuration parameters of the CoAX 600

Parameter	Value		
Gross weight	570 kg		
Maximum takeoff weight	600 kg		
Number of blades	2 upper, 2 lower		
Blade flapping inertia I_{β} (incl. the hub)	$24 \text{ kg} \cdot \text{m}^2$		
Rotor radius	3.25 m		
Airfoil	NACA 23012		
Linear twist	-7.65 deg		
Chord length	0.22 m		
Nominal rotor speed	455 RPM		
Reference CG position in the body-fixed frame $(r_{CG})_B$	$[0,0,0]^T$ m		
Position of the lower rotor with respect to the CG $(r_{GR1})_B$	$[0, 0, -0.72]^T$ m		
Position of the upper rotor with respect to the CG $(r_{GR2})_B$	$[0, 0, -1.364]^T$ m		
Reference helicopter inertia without rotors	$\begin{bmatrix} 180.203 & 0 & -52.085 \\ 0 & 342.746 & 0 \\ -52.085 & 0 & 254.334 \end{bmatrix} kg \cdot m^2$		



Fig. 6 Measurement of the control rod positions at the swashplate via tensioned cable potentiometers.

$$\theta_{\text{col}} = k_{\text{col}_0} + k_{\text{col}_1} P_1 + k_{\text{col}_2} P_2 + k_{\text{col}_3} P_3 \tag{54}$$

$$\theta_c = k_{c_1} P_1 + k_{c_2} P_2 + k_{c_3} P_3 \tag{55}$$

$$\theta_{s} = k_{s}, P_{1} + k_{s}, P_{2} + k_{s}, P_{3} \tag{56}$$

where P_1 , P_2 , and P_3 are the potentiometer measurements at the three pushrods of the lower swashplate, and the ks are the parameters of this static model that were estimated using the least-squares method described in Ref. [28]. Note that the cyclic and collective pitch controls determined above are applied to both the upper and lower rotors [via Eq. (6)], as the lower rotor swashplate controls the upper rotor swashplate using a set of pushrods. The yaw input, θ_{yaw} , which is additional collective input on the upper rotor, was modeled as a linear function of a potentiometer P_4 measuring the motion of the single pushrod, which affects the θ_{vaw} rotor input:

$$\theta_{\text{yaw}} = k_{\text{yaw}} P_4 \tag{57}$$

C. Practical Parameter Estimation Approach and Results

The estimated model parameters, as well as their standard deviations, are provided in Table 2. Figures 7 and 8 show the applied inputs in hover and the corresponding model outputs and flight data for hover. The inputs and outputs for maneuvers performed in forward flight are presented in Figs. 9 and 10. Roll, pitch, yaw, and collective maneuvers are provided for the hover flight conditions and doublet maneuvers for the roll, pitch, and vaw directions for forward flight. A total of eight maneuvers were used for parameter estimation in hover, of which only a subset are visualized in Figs. 7 and 8. Similarly, six maneuvers at a subset of the velocities mentioned in the beginning of this section were used for forward flight parameter estimation, of which three are presented in Figs. 9 and 10. The forward flight maneuvers used for parameter estimation were conducted at indicated airspeeds of 60 and 80 km/hr. The roll and pitch maneuver inputs in Figs. 7 and 9 show an off-axis excitation component as the flight tests were piloted, and controlling the stick purely in one direction could not be achieved by the pilot.

The simultaneous estimation of all of the model parameters was not feasible due to their high correlation in some flight regimes. Furthermore, it is not practical to estimate the aerodynamic parameters of the helicopter fuselage in the hover flight condition because of the small effects of these parameters at low aerodynamic velocities compared with the rotor system.

As a solution, a two-step process was used to estimate the aerodynamic parameters of the rotorcraft. In a first step, the aerodynamic parameters of the rotor system were estimated using hover flight data. The rotor-specific parameters were then fixed, and forward flight data were used to estimate the remaining parameters. This two-step process is justified since the fuselage aerodynamic forces can be neglected when the rotorcraft aerodynamic velocity is limited due to the dependency of these forces and moments on the dynamic pressure [see Eqs. (36) and (38)]. Therefore, in flight

Table 2 Estimated rotor and airframe model parameters

Table 2	Estimated rotor and airframe model parameters			
Component	Parameter	Value	Standard error	
Rotor	$C_{R_{l_0}}$	0.0200	0.0006	
	$C_{R_{l_{lpha}}}$	5.4700	0.0025	
	$C_{R_{d_0}}$	0.0068	0.0003	
	$C_{R_{d_lpha}}$	0	0.0049	
	$C_{R_{d_{lpha^2}}}$	0.2490	0.0024	
	c_{β} @ Hover	0.618 ^a		
	c_{β} @ Forward Flight	0.73^{a}		
	$C_{L_{lpha_A}}$	0.1650	0.0086	
	C_{D_0}	0.0304^{a}		
	$C_{D_{lpha_A}}$	-0.0615^{a}		
	C_{Q_0}	O^a		
	$C_{\mathcal{Q}_{eta_A}}$	-0.0689	0.0076	
	C_{Q_r}	0.1640	0.0360	
	$C_{Q_{\zeta}}$	2.0600	0.1282	
	C_{l_0}	O^a		
Airframe	$C_{l_{eta_A}}$	0.0000	0.0002	
	C_{l_p}	-0.0266	0.0007	
	C_{l_r}	0.0044	0.0015	
	$C_{l_{\zeta}}$	0.0154	0.0045	
	C_{m_0}	-0.0052^{a}		
	$C_{m_{lpha_A}}$	-0.0097	0.0001	
	C_{m_q}	-0.4690	0.0058	
	C_{n_0}	O^a		
	$C_{n_{eta_4}}$	0.0035	0.0001	
	C_{n_r}	-0.0397	0.0012	
	$C_{n_{\zeta}}$	-0.2140	0.0037	

^aParameter was fixed during the final optimization run, and no standard error was computed.

conditions near hover, the rotor can be considered as the sole source of the external forces and moments. Any influence of the forward flight on the rotor parameters, as well as the rotor–fuselage interactions, was lumped into the aerodynamic parameters attributed to the fuselage and the remainder of the aerodynamic (control) surfaces.

The deviations of the cyclic and pedal controls $(\delta\theta_{c_{\text{trim}}}, \delta\theta_{s_{\text{trim}}})$, and $\delta\theta_{\text{yaw}_{\text{trim}}})$ at the trim points were also considered as further unknown parameters. The trim controls in the simulation can deviate from flight data due to different trim conditions, such as wind [28] or a slightly different CG. Similarly, the longitudinal $(x_B$ direction) and lateral $(y_B$ direction) offsets of the CG with respect to the rotor shaft of the helicopter were estimated for each maneuver. Ref. [37] provides details of the Archangel Systems AHRS model, which was also used in this study. This model includes a gravity compensation in the n_z measurement when the sensor is stationary and level. Furthermore, the initial rotor flapping and inflow states (in case of forward flight) were also estimated together with the other parameters.

The position of the CG for the rotorcraft and the moments of inertia were initially determined based on a CAD model of the rotorcraft with simple 3D geometries representing the pilot and the instrumentation onboard. The CG position along the z_B axis and the moments of inertia were adjusted using hover flight data. The teetering rotor system does not allow the direct transfer of moments from the blades to the rotor shaft, except in the z_B direction (i.e., the rotor torque). Therefore, the roll and pitch moments acting at the CG of the helicopter are caused by the offset between the CG and the position of the teetering joint of each rotor along the z_B axis.

If the aerodynamic parameters of the rotor system are kept constant, the roll and pitch responses of the helicopter are a function

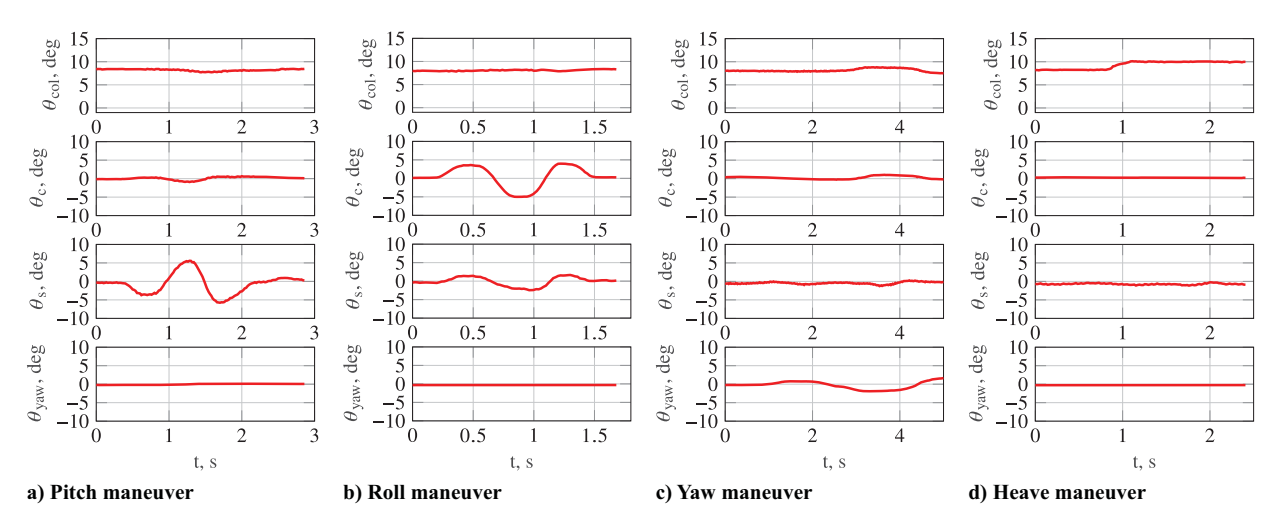


Fig. 7 Measured pilot inputs for the longitudinal and lateral maneuvers in hover.

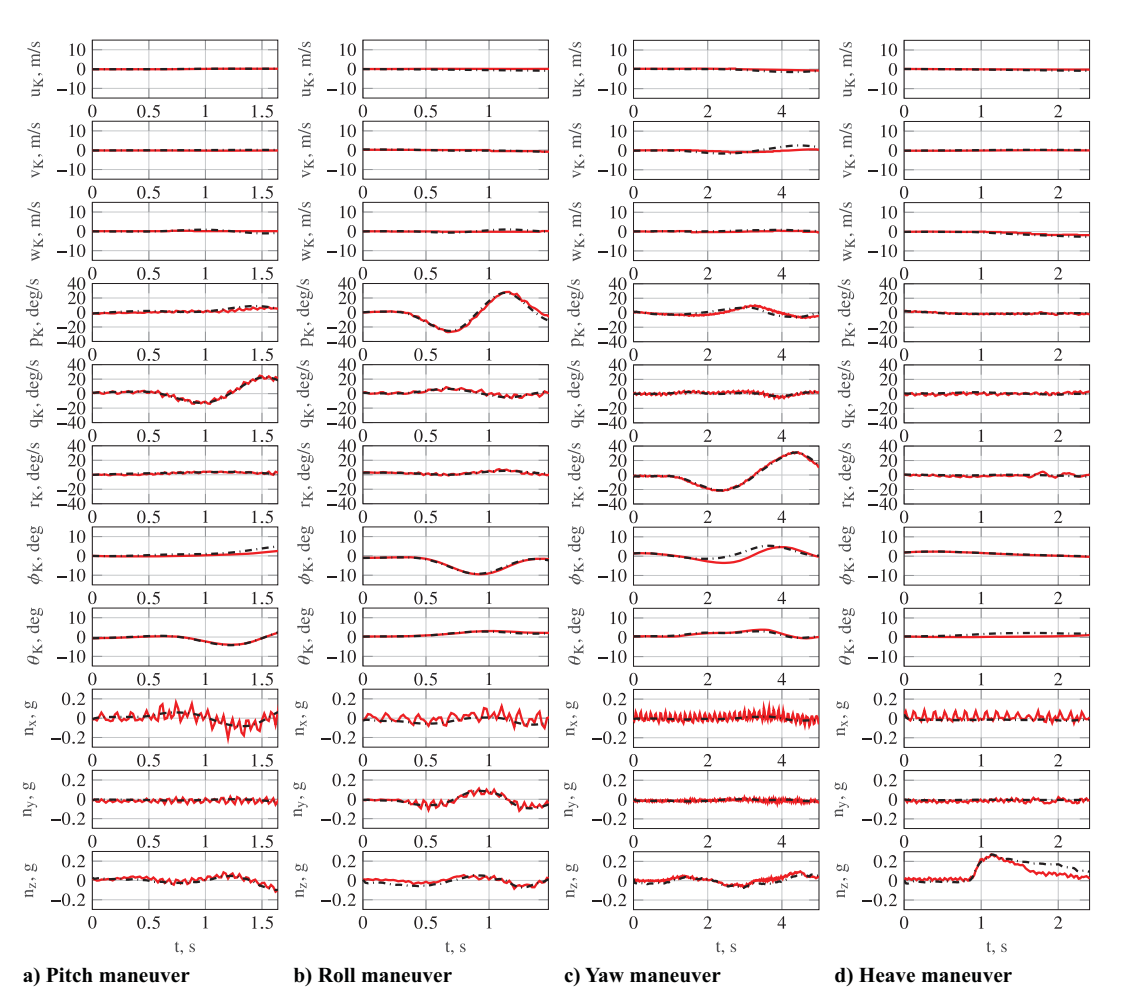


Fig. 8 Model response (black dash-dotted) and flight test data (red solid) in hover.

of the location of the CG and the roll and pitch moments of inertia of the helicopter fuselage. Since the mass of the helicopter was known, the rotor aerodynamic parameters of the rotor were initially estimated to ensure that the linear load factors n_x , n_y , and n_z (and therefore the forces produced by the rotor) were accurately represented by the model. It should be noted that while the rotor aerodynamic parameters do not change between different experiments, the CG position and the moments of inertia can vary due to different fuel tank fill levels. This fact was used to correct the CG position, as well as the roll and pitch moments of inertia, via different hover flight experiments. The estimation of the CG was additionally

supported by the studies of Refs. [37,41], which use flight path reconstruction using multiple accelerometers and simple kinematics equations to determine CG positions. The moment of inertia in the yaw direction was reduced with respect to the CAD model according to the same reduction factor as the moment of inertia values in the roll and pitch directions. This assumption relies on the observation that the same value was estimated for the reduction factors of I_{xx} and I_{yy} moments of inertia. Therefore, it was assumed that the actual I_{zz} will also have the same linear relation to its value from CAD. This has resulted in significant improvement of the model compared with the authors' previous work in Ref. [44]. This adjustment of the moments

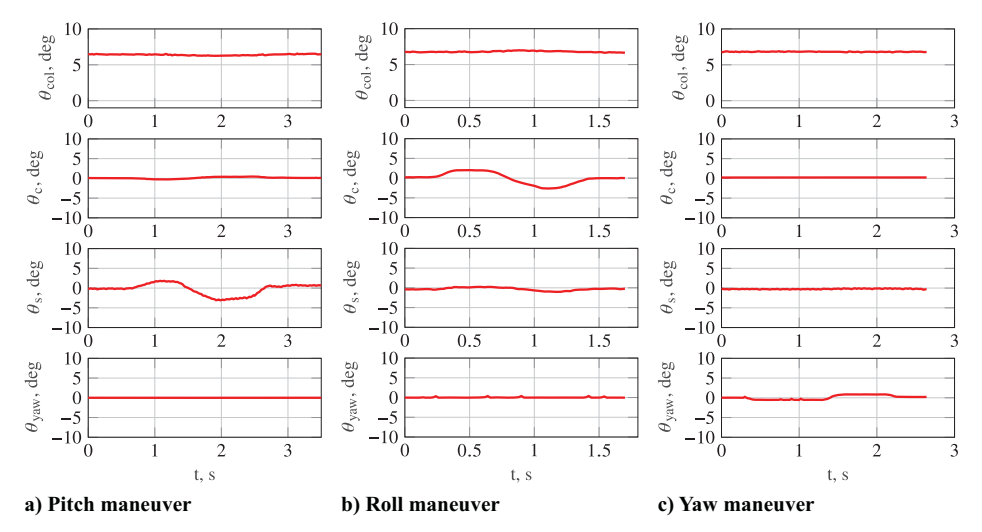


Fig. 9 Measured pilot inputs for the longitudinal and lateral maneuvers in forward flight.

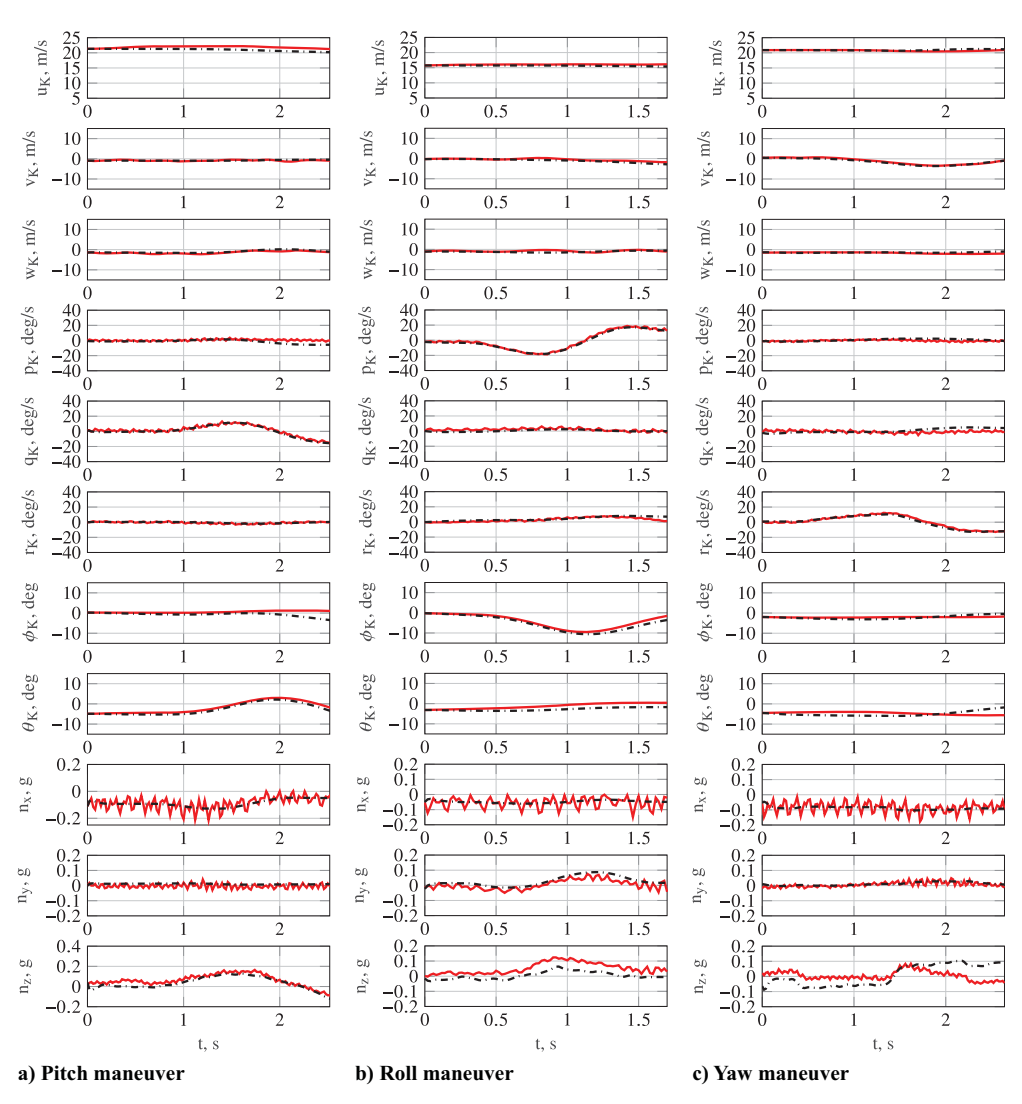


Fig. 10 Model response (black dash-dotted) and flight test data (red solid) in forward flight.

of inertia and the CG was based on the rotorcraft rate and linear acceleration response. While keeping the aerodynamic parameters of the rotor constant, the moments of inertia were estimated such that the rotorcraft rate response matched its acceleration response. Due to the teetering rotor system, the relation between the rate and the acceleration responses is only set by the moments of inertia and the

position of the center of gravity. The two-step strategy of estimating the moments of inertia while keeping the aerodynamic parameters fixed (and vice versa) was adopted since the simultaneous estimation of all parameters was not practical.

It was observed that the model overestimated the x_B and y_B linear acceleration responses of the rotorcraft as a response to the roll and

pitch maneuvers (cyclic inputs). The significant part of the aerodynamic force in hover, resulting in these accelerations, is caused by the tilting of the rotor tip path plane due to blade flapping. For a teetering rotor, the β_c and β_s flapping angles of each blade are equivalent to the cyclic inputs, i.e., $\beta_s = \theta_c$ and $\beta_c = \theta_s$. Since the mass of the rotorcraft was known, the overshoot in the linear accelerations meant that the two rotors tilted less than the theoretical value in response to a cyclic input by the pilot. A potential reason for this may be the fact that the rotor blades achieve a smaller cyclic pitch angle under load, meaning that the kinematic model that maps the control rod positions to the rotor pitch angles was not accurate while the rotor was rotating and under aerodynamic load. This phenomenon may come from the elasticity of the rotor blades around their torsion axis that was not modeled. The average change in the pitch angle over the blade radius during flight due to a cyclic input via the blade pitch links may be smaller than the static measurements of the blade pitch due to the stick inputs. The kinematic mapping of the stick to the blade pitch is described by Eq. (54), with parameters estimated from measurements on the nonrotating rotor. Since no flapping angles were measured in this study, the above physical reasoning could not be confirmed. This disagreement between the data and the model outputs was corrected by adjusting the pilot inputs via a linear factor c_{β} in Eq. (6). The rotorcraft moments of inertia were corrected subsequently for the rotational dynamics to also match the flight data. The values of the c_{β} parameter in hover and in forward flight are provided in Table 2.

The correction of the pilot inputs by the parameter c_{β} is warranted since the flight dynamics model inputs (rotor pitch angles according to cyclic commands) were estimated based on the measurement of the pushrod positions at the swashplate. The pushrod measurements are mapped to blade pitch angles via a static linear model discussed in Sec. V.B. This model was identified using static measurements on the nonrotating rotor. It is feasible that the effective cyclic rotor pitch angles during flight are lower due to aerodynamic and elastic effects at the rotor that were not explicitly modeled.

Leveraging the flight data in this study to estimate both the aerodynamic rotor parameters and the moments of inertia of the rotorcraft may result in inaccuracies in the estimated parameters despite the carefully selected method, as discussed above. These potential correlation effects were not quantified. The relaxed view of the moments of inertia in this study renders some of the estimated parameters physically less meaningful. Inaccuracies in the estimated values for the moments of inertia (e.g., due to violated assumptions) will result in physically incorrect aerodynamic parameter values. However, the nonlinear model still accurately models the rotorcraft (see Figs. 8 and 10) and can (together with the linearized models)

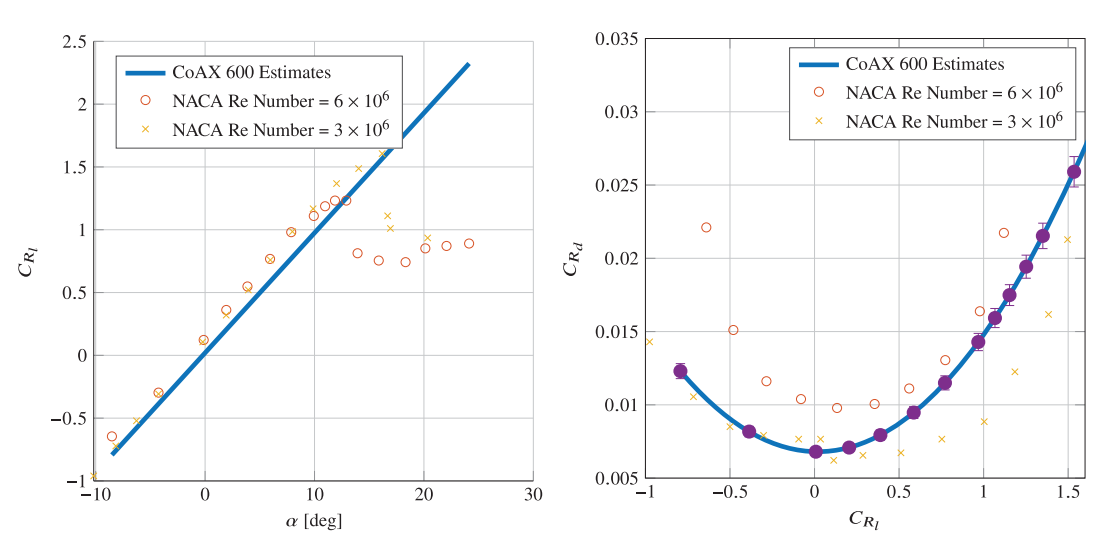
serve the control design and pilot training purposes well. Reference [45] gives a comprehensive overview of the consequences of parameter estimation using a nonlinear model structure with unknown mass properties.

The blade airfoil aerodynamic parameters $C_{R_{d_0}}$, $C_{R_{d_a}}$, and $C_{R_{d_a}}$ were estimated from flight data in this study. This is in contrast to other physics-based rotorcraft modeling frameworks, where aerodynamic look-up tables, developed via theoretical methods or wind tunnel tests, are used in the model to represent the blade aerodynamics. The feasibility of the blade airfoil aerodynamic parameter estimates was verified by comparing the computed engine power during hover and collective lever step maneuvers (see Fig. 8d) with the available engine power onboard the helicopter. The maximum engine power during the collective step input was used as a constraint during the collective step maneuver while estimating the rotor profile drag parameters. Figure 11 compares the estimates of the airfoil parameters in this study with the measurements of the NACA 23012 airfoil, digitized from Ref. [46]. The figure includes two sets of lift and drag measurements, at the chord Reynolds numbers of 3×10^6 and 6×10^6 . The measurements at the higher chord Reynolds numbers were conducted at standard roughness, where 0.011 in carborundum grains were applied to the surface of the model at the leading edge over a surface length of 0.08 c measured from the leading edge on both sides, where c refers to the chord length of the airfoil. The CoAX 600 rotor blades operate at an average chord Reynolds number of 1.133×10^6 .

The lift and drag curves are mostly in agreement with the NACA measurements. It can be seen that both the lift curve slope C_{l_a} and the lift at zero angle of attack C_{l_0} are slightly lower than the NACA measurements. This is reasonable since the effects, such as the finite blade length, rotor–body interactions, and stall, were not explicitly modeled in this study. The loss of the effective lift produced by the rotor system is therefore reflected in the parameter estimates.

The drag curve with the estimated CoAX 600 rotor blade parameters lies between the two NACA measurements. The real-world effects mentioned above will also cause the estimated drag for a given lift coefficient C_l to be higher. It can be inferred from Fig. 11 that the lower chord Reynolds number and the mentioned unmodeled aerodynamic effects do not cause drag as much as the standard roughness of NACA measurements. However, it should be noted that the drag coefficient estimates mostly depend on the yaw maneuvers and therefore also on the yaw moment of inertia of the airframe. Inaccuracies of the values for the moments of inertia result in biased estimates of the drag parameters.

As mentioned before, not all of the parameters in Table 2 were estimated simultaneously. The rotor-system-related parameters were estimated using hover data, while the remainder of the parameters



a) Lift coefficient vs. airfoil angle of attack

b) Drag coefficient vs. lift coefficient

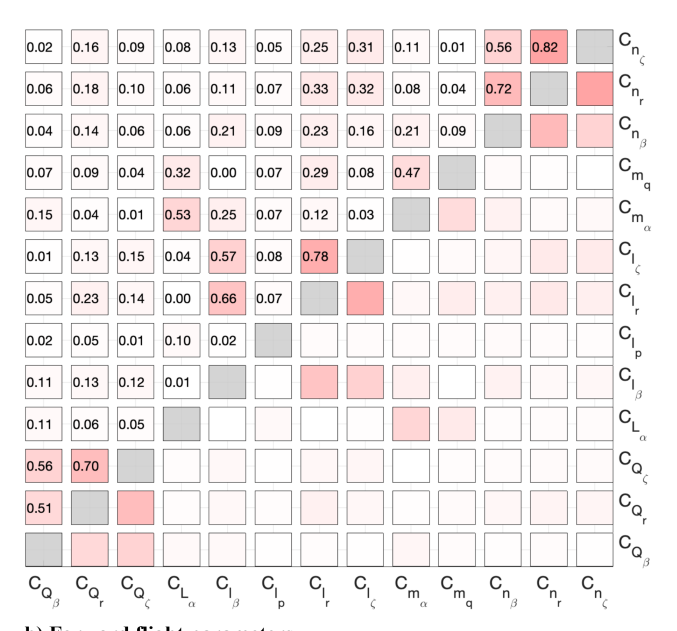
Fig. 11 Airfoil lift and drag estimates with NACA measurements.

were estimated using forward flight data. This should be kept in mind when interpreting the standard deviation values provided in Table 2. The parameters C_{D_0} , $C_{D_{a_A}}$, and C_{m_0} were determined separately by matching the model trim inputs and states during forward flights of different velocities over the runway (with no excitations) to flight data.

The correlations between the parameters of each parameter group estimated together is visualized in Fig. 12. Each plot visualizes the absolute values of the respective parameter correlation matrices. The parameter correlations remain below the 0.9 rule of thumb [28]. Figures 8 and 10 also show that the initial n_x , n_y , and n_z of the rotorcraft is inaccurate for some of the experiments. The deviation from the overall trend in the beginning of the maneuver mostly results from the terms in Eq. (1) not related to aerodynamic forces and moments. Estimating the initial states together with the model parameters theoretically solves this issue. However, it led to convergence issues during the numerical optimization. The highfrequency oscillations in the n_x , n_y measurements are attributed to the vibrations in the mounting platform of the IMU on the rotorcraft. These vibrations, which were induced by the rotor at its rotational frequency, were not modeled since the rotor forces and moments were averaged over a full rotor revolution at each simulation time step, as explained in Sec. III. No standard deviation is provided for



a) Hover parameters



b) Forward flight parameters

Fig. 12 Absolute values of the correlation matrices.

the parameters that were set as fixed in the final optimization setup or determined via a constraint. The coefficient of determination R^2 as described in Ref. [28] was computed for the on-axis rate responses in hover. The coefficient of determination can be interpreted as the ratio of the part of the system response variation that the model covers to the total variation of the measured system response. For each rate response, it was computed using the maneuvers in Fig. 8 and an additional maneuver that was not included for system identification but from the same maneuver batch, executed immediately after each other. The coefficient of determination is $R_{\rm roll}^2 = 0.937$ for the roll maneuvers, $R_{\rm pitch}^2 = 0.949$ for the pitch maneuvers, and $R_{\rm vaw}^2 = 0.994$ for the yaw maneuver.

The nonlinear simulation model can be linearized at any trim point of the flight envelope. The rotor flapping motion and the inflow were considered as quasi-static systems for the purpose of linearization such that the linear model only includes the rigid body states. The poles of the current linear rigid body models in hover are visualized in Fig. 13. As expected, the helicopter is unstable in hover. The linearization results were verified in a parallel study [37] in which a linear model of the rotorcraft was estimated from the same flight data set. The linearized model shows good agreement with the linear model of [37].

In summary, the parameter estimation steps were the following:

- 1) The first step is the estimation of the rotor system aerodynamic parameters $C_{R_{l_0}}$, $C_{R_{l_a}}$, $C_{R_{d_0}}$, $C_{R_{d_a}}$, and $C_{R_{d_{a^2}}}$ from flight data while keeping the correction factors of the moments of inertia fixed. The fuselage aerodynamic parameters were also set as fixed.
- 2) While keeping all other parameters fixed, the pilot input correction factor c_{β} was estimated such that the model linear accelerations matched the flight data. Other outputs were not considered at this step.
- 3) Correction factors for the moments of inertia were estimated using hover flight data such that the rotorcraft rate response matched the flight data as well. This was done while keeping the aerodynamic rotor system parameters and the pilot input correction factor c_{β} fixed.
- 4) The first three steps were repeated until all of the model outputs were in agreement with the flight data, while making sure that the rotor power in hover was reasonable when compared with the engine settings.
- 5) The fuselage aerodynamic parameters were estimated using forward flight data.

It is evident from the above summary that the applied relaxation strategies may result in biased and physically less meaningful parameter values. However, the overall behavior of the model still remains valid as seen from the model match. Furthermore, a more accurate model of the mass properties and the measurement of the rotor flapping angles would have eliminated the need for the relaxations and simplifications applied in this study.

V. Control Design

Figure 13 shows that the CoAX 600 rotorcraft simulation model is unstable in the hover flight condition. A human pilot sitting in the helicopter is capable of controlling the helicopter using only the mechanical controls, despite the instability of the system. However, the observations during the hardware-in-the-loop tests reported in [2] showed that controlling the rotorcraft remotely using the onboard actuator system was very difficult in open loop. The actuator dynamics and the signal transport delays in the sensor signals and actuator commands make the operation of the CoAX 600 rotorcraft barely possible for the remote pilot. Pilot-in-the-loop oscillations are easily induced due to the delays.

A linear attitude controller was developed in this study as an intermediate step toward a fully automatic flight control system. The control law for the roll and pitch motion of the rotorcraft is visualized in Fig. 14. The roll and pitch angles (ϕ, θ) , as well as the roll and pitch rates (p, q), are used as feedback signals to stabilize the helicopter. The yaw control law (depicted in Fig. 15) is slightly different. In this case, a proportional-integral (PI) control law was

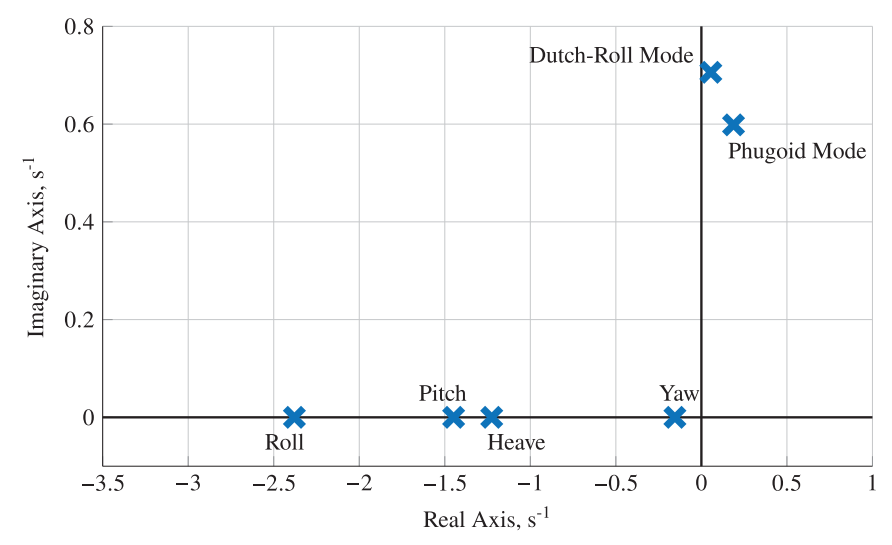


Fig. 13 Poles of the CoAX 600 rotorcraft simulation model, linearized in hover.

Actuator Cutoff Position for Stability Analysis $k_{\theta_c,\theta_s} = k_{\theta_c,\theta_s} + k_{\theta_c,\theta$

Fig. 14 CoAX UAS flight control law for the roll and pitch rotational motions.

Actuator Cutoff Position for Stability Analysis $k_{\theta_{yaw}} \xrightarrow{\theta_{yaw_p}} ACT \xrightarrow{ADA} Low Pass \\ \hline Filter$ Pilot stick input

Integrator block with output saturation k_r

Fig. 15 CoAX UAS flight control law for yaw rotation.

applied to the yaw feedback to increase the damping in the yaw dynamics and allow for steady-state accuracy of the yaw rate. All of the inertial measurements were low-pass-filtered with a cutoff frequency lower than the rotor RPM.

The control laws from Figs. 14 and 15 are

$$\theta_c = \theta_{c_p} - k_p p - k_\phi \phi \tag{58}$$

$$\theta_s = \theta_{s_p} - k_q q - k_\theta \theta \tag{59}$$

$$\theta_{\text{yaw}} = \theta_{\text{yaw}_p} - k_r r + \frac{1}{s} k_{\psi} (\theta_{\text{yaw}_p} - k_r r)$$
 (60)

A linear mapping exists between the remote controller stick deflections and the pilot inputs θ_{c_n} , θ_{s_n} , and θ_{yaw_n} at the swashplate.

All of the nonlinearities in the mechanical linkages and the actuators were canceled via look-up tables (LuTs) as described in [2].

The feedback gains were designed based on a truncated version of the linear model. The translational velocity and the position states were omitted because the inner-loop controller only addresses the rotational motion of the rotorcraft. The state and input vectors of the truncated model are

$$\mathbf{x} = [p, q, r, \phi, \theta]^T \tag{61}$$

$$\boldsymbol{u} = [\theta_c, \theta_s, \theta_{\text{vaw}}]^T \tag{62}$$

The linearized model of the CoAX 600 in hover (with its pole-zero-map shown in Fig. 13) was used to determine the truncated

model mentioned above. Consequently, the rotor and inflow dynamics were considered as steady state. The low-pass filters as depicted in Figs. 14 and 15 are second-order linear time-invariant systems, implemented to filter the rotor vibrations. The dynamics of the actuators and the inertial sensors (AHRS) were modeled as first-order linear systems with signal transport delays as follows:

$$Y(s) = \frac{k}{1 + T_f s} e^{-T_d s}$$
 (63)

The time constants and the input delays of the mentioned transfer functions were chosen to account for the worst-case phase and dead-time delays caused by the sensor internal dynamics and filters and the actuator and rotor dynamics. The Archangel ADARHS was modeled as a first-order filter based on test data captured on a turntable. Reference [2] also describes the estimation of the actuator models. Both the input delays and the time constants for the mentioned transfer functions were increased by a safety margin factor to account for the rotor dynamics and possible inaccuracies in the estimated actuator parameters. The time delays are caused by the avionics system.

The stability and robustness analysis was performed by means of loop transfer functions at the actuator cuts, as shown in Figs. 14 and 15. The closed-loop system was cut at each of the actuator command signals to create the SISO transfer functions $G_{l_{\theta_y aw}\theta_y aw}$. The closed-loop system poles of the rotational motion are given in Fig. 16. The fast poles and zeros resulting from the actuator and rotor dynamics are excluded from the plot. The structure of the poles related to the closed-loop rate response of the rotorcraft as seen in Fig. 16 differs from the open-loop rate responses. Specifically, new poles are added due to the introduced actuator and sensor dynamics, together with the feedback loops. Each pole in Fig. 16 is noted with the significant states prevalent in the respective eigendynamics.

The response of the system to a unit step input is shown in Fig. 17. The gain and phase margin as provided in Table 3 satisfy and exceed the 6 dB gain margin and the 45 deg phase margin limits required by ADS-33 [47]. It should be noted that the values in Table 3, especially the phase margins, are pessimistic since safety factors were applied to the input delays and the time constants of the transfer functions in the control loops of Figs. 14 and 15.

It can be seen that the closed-loop poles of the truncated system [with the states of the Eq. (61)] have faster and well-damped poles. The faster dynamics with the increased damping resulted in significantly improved handling qualities for a human pilot. Furthermore,

the attitude control and the ability of the helicopter to maintain its attitude for a short time after external disturbances reduced the remote pilot's workload. The flight control laws developed in this work were tested in a flight test campaign at the Magdeburg-Cochstedt Airport (EDBC) in Germany, as reported in Ref. [2]. A total of four unmanned flight hours were accumulated.

VI. Conclusions

A physics-based nonlinear model of the full-scale CoAX 600 rotorcraft was developed. Parameter estimation techniques were applied to estimate the values of the unknown model parameters using flight test data. The model was used for the design and tuning of an attitude controller for hover and slow forward flight. The nonlinear model was linearized at the hover trim point for this purpose. The linear model was first simplified by considering the rotor and inflow states as steady state, such that only the rigid-body states, excluding the geographic longitude and latitude, were included in the linear model. The model was further truncated for the purpose of control design such that only the rotational dynamics were considered.

The values for the aerodynamic parameters of the nonlinear model were estimated from flight data using an optimal control-based implementation of the Maximum-Likelihood parameter estimation method in the time domain. Proof of matches was provided for hover and forward flight in the time domain. Accurate measurements of the helicopter mass properties were not available. Therefore, these were determined from flight data, and their accuracy cannot be independently validated. This should be kept in mind for any physical interpretation of the estimated aerodynamic parameters of the rotorcraft. The main advantages of the rotorcraft modeling and system identification approach in this study, which relies on a physics-based model structure and parameter estimation in the time domain, are the following:

- 1) Fewer unknown parameters to be estimated from flight test data, especially in hover, when compared with traditional linear model identification methods
- 2) Global nature of the model and the possibility of model linearization at different points of the flight envelope
- 3) A more realistic feel when deployed to manned flight simulators due to the simulation of the rotor rotation and the rotor inflow
- 4) Easier physical interpretation of the parameters based on the knowledge of the helicopter flight physics
- 5) Modularity of the model and the possibility to further extend its fidelity, e.g., by including a more sophisticated inflow model or a blade aeroelastic model

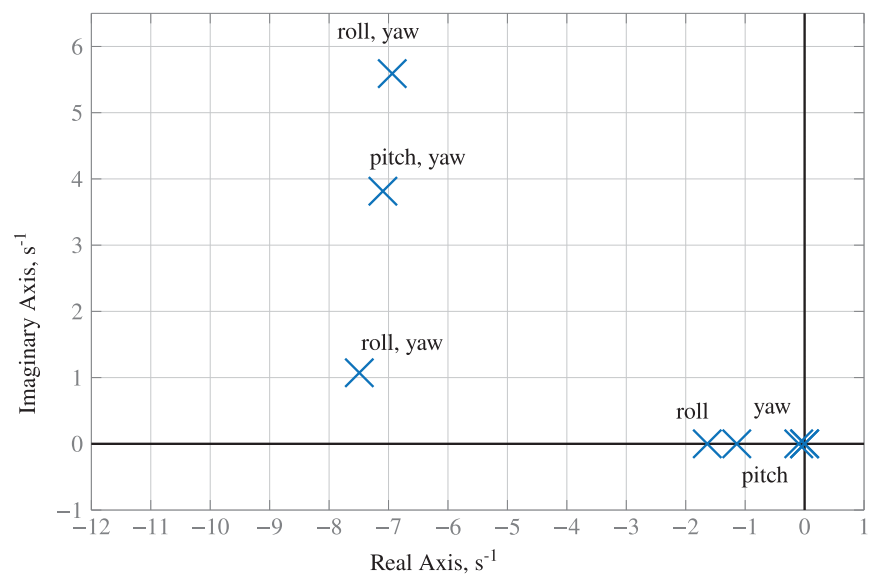


Fig. 16 Closed-loop dynamic system poles.

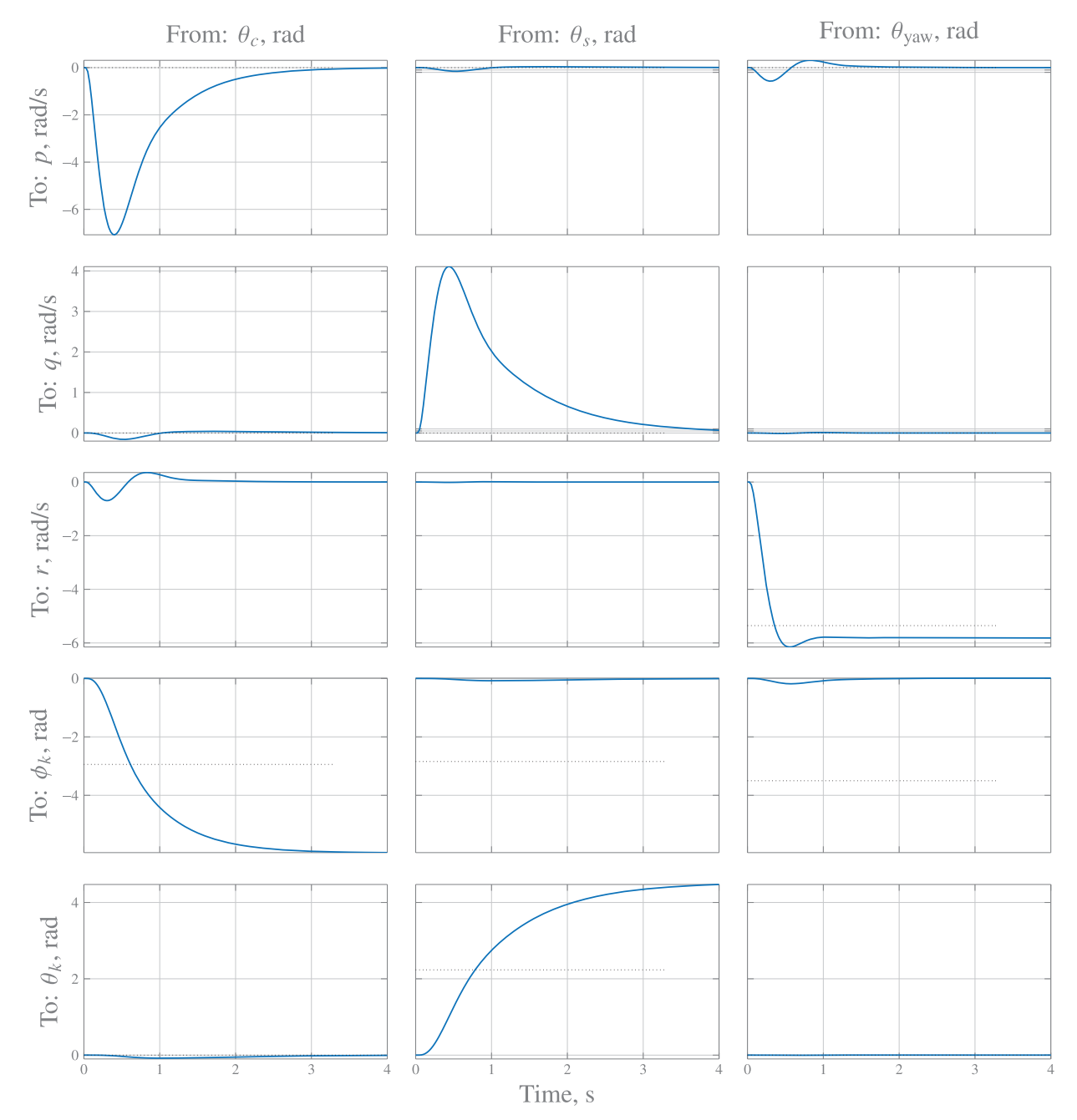


Fig. 17 Closed-loop system unit step response.

Table 3 Phase and gain margins

Loop transfer function	Gain margin, dB	Phase margin, deg
$\overline{G_{l_{ heta_c} heta_c}}$	11.19	61.6
$G_{l_{ heta_s} heta_s}$	11.1	57.54
$G_{l_{ heta_{yaw} heta_{yaw}}}$	11.21	61.94

The main disadvantage of the developed rotorcraft modeling and parameter estimation method in this study is the high implementation burden compared to other more common methods.

A linear attitude controller, as described in Sec. VI, was developed and tuned using the developed flight dynamics model to reduce the remote pilot workload. The remote operation of the rotorcraft via the developed flight control system was not possible without a feedback controller due to the actuator dynamics and the dead-time delays in the system caused by the avionics. The aircraft with the closed-loop attitude controller showed excellent flying qualities and robustness during the uncrewed flight tests, even in

windy weather with significant gusts. The proofs of matches for the model, as well as the successful unmanned flight tests, demonstrated the effectiveness of the approaches used in this study.

Acknowledgments

The flight test data for this research were measured and contributed by the Technical University of Munich.

References

- [1] Edm Aerotec GmbH Web," Online, 2021, https://edm-aerotec.de/en/ [retrieved 18 May 2024].
- [2] Hosseini, B., Rhein, J., Holzapfel, F., Grebing, B., and Rauleder, J., "Conversion of a Coaxial Rotorcraft to a UAV–Lessons Learned," *Aerospace*, Vol. 11, No. 8, 2024, p. 681. https://doi.org/10.3390/aerospace11080681
- [3] Göttlicher, C., "System Identification for Aerial Applications Using Optimal Control Methods," Dissertation, Technische Universität München, Munich, Germany, 2019, http://mediatum.ub.tum.de/node? id=1471018.

- [4] Leishman, G., Principles of Helicopter Aerodynamics, 2nd ed., Cambridge Univ. Press, New York, 2006.
- [5] Padfield, G., Helicopter Flight Dynamics, 2nd ed., Blackwell Science Ltd., Oxford, U.K., 2007.
- [6] "Advanced Rotorcraft Technology," Online, 2017, https://www. flightlab.com [retrieved 18 May 2024].
- [7] Du Val, W., and He, C., "Validation of the FLIGHTLAB Virtual Engineering Toolset," *Aeronautical Journal*, Vol. 122, No. 1250, 2018, pp. 519–555. https://doi.org/10.1017/aer.2018.12
- [8] Padfield, G., and White, M., "Flight Simulation in Academia HELI-FLIGHT in Its First Year of Operation at the University of Liverpool," Aeronautical Journal, Vol. 107, No. 1075, 2003, pp. 529–538. https://doi.org/10.1017/S0001924000013415
- [9] Saberi, H., Hasbun, M., Hong, J., Yeo, H., and Ormiston, R. A., "Overview of RCAS Capabilities, Validations, and Rotorcraft Applications," *American Helicopter Society 71st Annual Forum Proceedings*, 2015.
- [10] Johnson, W., "Technology Drivers in the Development of CAMRAD II," American Helicopter Society Aeromechanics Specialist Meeting, American Helicopter Soc., Alexandria, VA, Jan. 1994.
- [11] "CAMRAD II Software Description," Online, 2023, https://johnson-aeronautics.com/CAMRADII.html [retrieved 6 June 2023].
- [12] Tischler, M., and Remple, R., Aircraft and Rotorcraft System Identification: Engineering Methods with Flight Test Examples, AIAA, Reston, VA., 2006.
- [13] CasalCorp, "CIFER: Comprehensive Identification from Frequency Responses, Software User's Manual," Online, 2005, http://casalcorp. com/images/CIFER_Users_Manual_V4-2-00_part_one_.pdf [retrieved 18 May 2024].
- [14] Tischler, M. B., and Cauffman, M. G., "Frequency-Response Method for Rotorcraft System Identification: Flight Applications to BO-105 Coupled Fuselage/Rotor Dynamics," *Journal of the American Helicopter Society*, Vol. 37, No. 3, 1992, pp. 3–17. https://doi.org/10.4050/JAHS.37.3.3
- [15] Mettler, B., Tischler, M. B., and Kanade, T., "System Identification of Small-Size Unmanned Helicopter Dynamics," *American Helicopter Society 55th Annual Forum Proceedings*, American Helicopter Soc., Alexandria, VA, May 1999.
- [16] Cho, S. H., Bhandari, S., Sanders, F. C., Cheung, K. K., and Tischler, M. B., "System Identification and Controller Optimization of a Coaxial Quadrotor UAV in Hover," *AIAA SciTech Forum*, AIAA Paper 2019-1075, 2019. https://doi.org/10.2514/6.2019-1075
- [17] Cicolani, L., McCoy, A., Tischler, M., Tucker, G., Gatenio, P., and Marmar, D., "Flight-Time Identification of a UH-60A Helicopter and Slung Load," NASA TM-1998-112231, 1998.
- [18] Lawler, M., Ivler, C., Tischler, M., and Shtessel, Y., "System Identification of the Longitudinal/Heave Dynamics for a Tandem-Rotor Helicopter Including Higher-Order Dynamics," AIAA Atmospheric Flight Mechanics Conference and Exhibit, AIAA Paper 2006-6147, 2006. https://doi.org/10.2514/6.2006-6147
- [19] Tischler, M., and Tobias, E., "A Model Stitching Architecture for Continuous Full Flight-Envelope Simulation of Fixed-Wing Aircraft and Rotorcraft from Discrete Point Linear Models," Aviation and Missile Research, Development and Engineering Center Redstone Arsenal United States, Defense Technical Information Center (DTIC), 2016.
 - https://doi.org/10.21236/AD1008448
- [20] Zivan, L., and Tischler, M., "Development of a Full Flight Envelope Helicoter Simulation Using System Identification," *Journal of the American Helicopter Society*, Vol. 55, No. 2, 2010, Paper 22003. https://doi.org/10.4050/JAHS.55.022003
- [21] Seher-Weiss, S., Greiser, S., Wartmann, J., Gubbels, A., Ricciardi, J., and Hui, K., "Bell 412 System Identification: Comparing Methods and Tools," AHS International 75th Annual Forum, American Helicopter Soc., Fairfax, VA, May 2019, Paper 14636.
- [22] Hamel, P., and Kaletka, J., "Advances in Rotorcraft System Identification," *Progress in Aerospace Sciences*, Vol. 33, No. 3, 1997, pp. 259–284. https://doi.org/10.1016/S0376-0421(96)00005-X
- [23] Wartmann, J., and Seher-Weiss, S., "Application of the Predictor-Based Subspace Identification Method to Rotorcraft System Identification," 39th European Rotorcraft Forum, Sept. 2013, Paper erf2013_007.
- [24] Seher-Weiss, S., "ACT/FHS System Identification Including Rotor and Engine Dynamics," *Journal of the American Helicopter Society*, Vol. 64, No. 2, 2019, pp. 1–12. https://doi.org/10.4050/JAHS.64.022003
- [25] Grauer, J., Conroy, J., Hubbard, J., Jr., and Pines, D., "System Identification of a Miniature Helicopter," *Journal of Aircraft*, Vol. 46,

- No. 4, 2009, pp. 1260–1269. https://doi.org/10.2514/1.40561
- [26] Padfield, G., Thorne, R., Murray-Smith, D., Black, C., and Caldwell, A., "UK Research into System Identification for Helicopter Flight Mechanics," *Vertica*, Vol. 11, No. 4, 1995, pp. 270–277. 1987, pp. 665–684.
- [27] Schafroth, D., Bermes, C., Bouabdallah, S., and Siegwart, R., Modeling and System Identification of the muFly Micro Helicopter, Springer Netherlands, Dordrecht, 2010, pp. 27–47.
- [28] Morelli, E. A., and Klein, V., Aircraft System Identification: Theory and Practice, 2nd ed., Sunflyte Enterprises, Williamsburg, VA, 2016.
- [29] Morelli, E. A., "Real-Time Global Nonlinear Aerodynamic Modeling for Learn-to-Fly," AIAA Atmospheric Flight Mechanics Conference, AIAA Paper 2016-2010, 2016. https://doi.org/10.2514/6.2016-2010
- [30] Morelli, E. A., "Global Nonlinear Aerodynamic Modeling Using Multivariate Orthogonal Functions," *Journal of Aircraft*, Vol. 32, No. 2, 1995, pp. 270–277. https://doi.org/10.2514/3.46712
- [31] Kong, Y. B., "Development of a Finite State Coaxial Rotor Dynamic Inflow Model," Ph.D. Dissertation, Georgia Inst. of Technology, Atlanta. GA, 2018.
- [32] Bachfischer, M., Hosseini, B., and Holzapfel, F., "Development and Validation of an Inflow Model for a Coaxial Teetering Rotor System, AIAA Aviation Forum, AIAA Paper 2022-3685, 2022. https://doi.org/10.2514/6.2022-3685
- [33] Ruh, M., and Hwang, J., "Robust Modeling and Optimal Design of Rotors Using Blade Element Momentum Theory," AIAA Aviation Forum, AIAA Paper 2021-2598, 2021. https://doi.org/10.2514/6.2021-2598
- [34] Chen, R., "A Survey of Nonuniform Inflow Models for Rotorcraft Flight Dynamics and Control Applications," NASA TM 102219, NASA Ames Research Center, Moffett Field, CA, 1989.
- [35] Anon., U.S. Standard Atmosphere, NASA and USAF and USWB, Washington, D.C., 1962.
- [36] Press, W. H., Teukolsky, S. A., Vetterling, W. T., and Flannery, B. P., Numerical Recipes: The Art of Scientific Computing, 3rd ed., Cambridge Univ. Press, New York, 1992.
- [37] Bachfischer, M., Hosseini, B., and Holzapfel, F., "Linear Model Identification for a Coaxial Rotorcraft in Hover," AIAA SciTech Forum, AIAA Paper 2024-1719, 2024. https://doi.org/10.2514/6.2024-1719
- [38] Jategaonkar, R. V., Flight Vehicle System Identification: A Time Domain Methodology, AIAA, Reston, VA, 2006.
- [39] Hosseini, B., Steinert, A., Hofmann, R., Fang, X., Steffensen, R., Holzapfel, F., and Göttlicher, C., "Advancements in the Theory and Practice of Flight Vehicle System Identification," *Journal of Aircraft*, Vol. 60, No. 5, 2023, pp. 1419–1436. https://doi.org/10.2514/1.C037269
- [40] Maier, L., Hosseini, B., Barth, A., Holzapfel, F., and Hajek, M., "On the Flight Test Campaign of a Coaxial Helicopter for the Development of an Unmanned Aerial System," AIAA Aviation Forum, AIAA Paper 2022-3557, 2022. https://doi.org/10.2514/6.2022-3557
- [41] Hofmann, R., Hosseini, B., Fang, X., Rhein, J., Sax, F., Holzapfel, F., Maier, L., and Barth, A., "Center of Gravity Estimation Using Multiple Accelerometers," AIAA SciTech Forum, AIAA Paper 2024-1721, 2024.
- [42] "Archangel Systems AHR150A/300A," Online, 2021, https://archangel.com/products/ahr150-300adahrs [retrieved 18 May 2024].
- [43] "NexNav MAX GPS SBAS Sensor Units (GPSSU)," Online, 2022, https://aspennexnav.com/products/?cat=gpssu#max-gpssu [retrieved 18 May 2024].
- [44] Hosseini, B., Sax, F., Rhein, J., Holzapfel, F., Maier, L., Barth, A., Hajek, M., and Grebing, B., "Global Model Identification for a Coaxial Helicopter," VFS Forum, Vol. 78, May 2022, pp. 1–11. https://doi.org/10.4050/F-0078-2022-17575
- [45] Simmons, B., Gresham, J., and Woolsey, C., "Nonlinear Dynamic Modeling for Aircraft with Unknown Mass Properties Using Flight Data," *Journal of Aircraft*, Vol. 60, No. 3, 2023, pp. 968–980. https://doi.org/10.2514/1.C037259
- [46] Abbott, I., and von Doenhoff, A., *Theory of Wing Sections: Including a Summary of Airfoil Data*, Dover Publ., New York, 1959.
- [47] Anon., ADS-33, "Aeronautical Design Standard, Handling Qualities Requirements for Military Rotorcraft," U.S. Army Aviation and Missile Command, Aviation Engineering Directorate, Redstone Arsenal, Alabama, 2000.